

Oxidation of additively manufactured Ni-base alloy IN625: mechanism of intergranular oxidation

A. Chyrkin^{1,a}, A. Fazi^{2,b}, M. Sattari², D. Mayweg², M. Thuvander², K. Stiller²,
M. Halvarsson², W.J. Nowak³, E. Wessel⁴, D. Naumenko⁴, J. Froitzheim¹

- 1) *Chalmers University of Technology, Department of Chemistry and Chemical Engineering, Kemivägen 10, 412 96, Gothenburg, Sweden*
- 2) *Chalmers University of Technology, Department of Physics, Kemigården 1, 412 96, Gothenburg, Sweden*
- 3) *Rzeszow University of Technology, Faculty of Mechanical Engineering and Aeronautics, Department of Materials Science, al. Powstanców Warszawy 12, 35-959 Rzeszow, Poland*
- 4) *Forschungszentrum Jülich GmbH, Institute for Energy Materials and Devices (IMD-1), Leo-Brandt-Straße, 524 25 Jülich, Germany*

Abstract

The oxidation resistance of additively manufactured (AM) Ni-base alloy Inconel 625 (IN625) has been evaluated in air at 900 °C and compared with that of the conventionally manufactured (CM) forged alloy. The AM alloy suffered from intergranular oxidation (IGO) in contrast to CM. The Cr₂O₃ scales thermally grown on both CM and AM were analyzed with SEM/EDX, EBSD, GD-OES, TEM and APT. A new mechanism of IGO in AM alloys is proposed. Oxide scale decohesion over the alloy grain boundaries is believed to be the key trigger of IGO originating from minor differences in the alloy compositions (Al, Mn, Si, Ti) between AM and CM, rather than the AM process itself.

^a Corresponding author

E-mail: chyrkin@chalmers.se

^b current address: Department of Nuclear Science and Engineering, Massachusetts Institute of Technology, Cambridge, MA, USA

INTRODUCTION

Ni-base superalloys are state-of-the-art structural materials for high-temperature applications requiring both high creep strength and environmental resistance, e.g., in power generation, jet-engine technology, petrochemical industry, nuclear technologies, heat processing, etc. [1].

Additive manufacturing (AM) of high-temperature alloys has been booming in the past decade, especially in aeronautics, where AM offers a significant flexibility of shaping components as well as decreasing material waste [2–6]. The wrought Ni-base alloy IN625 is a well-established, commercially available Ni-base superalloy widely studied in AM [5]. The creep strength of AM alloy IN625 [7,8] has been reported to be close to that of the conventionally manufactured (CM) alloy IN625. At the same time, the oxidation resistance of AM IN625 [9–21] and IN718, a further development of IN625 based on the same strengthening concept, [22–25] is systematically inferior to that of CM. The following empirical observations can be summarized based on the available literature:

- I) AM alloys usually oxidize 25–30% faster than CM.
- II) No oxidation rate anisotropy has been reported.
- III) AM Ni-base alloys suffer from intergranular oxidation (IGO) attack.

In our previous publications [12,13], AM alloy IN625 was shown to suffer from IGO attack in agreement with literature [9–11,14,16–19,21]. Changing the alloy microstructure via homogenization heat-treatments and/or hot-rolling to recrystallize the alloy did not affect the oxide scale morphology [12]. IGO was thus believed to originate from minor differences in chemical composition between the tested batches of AM and CM within the specification, i.e., the Si content in AM was a factor of 3 lower compared to that in CM [13]. At the same time, the exact role of the missing Si in the IGO of AM alloy IN625 remained rather vague, while the mechanism and triggers of IGO in AM Ni-base alloys are still lively discussed in the literature [9–11,22,23]. It is still unclear where exactly IGO is initiated: the Cr₂O₃ scale, the underlying AM metal, the oxide-metal interface, alloy grain boundaries (GBs), IG voids, etc. Furthermore, a study involving an AM and a CM alloy with as identical chemical compositions as practically possible (composition may change

during the AM process) would be the best way to prove the batch-to-batch variation hypothesis.

In the present work, a special emphasis was put on a comprehensive microstructural characterization of the thermally grown Cr₂O₃ scale to better understand the origin of the differences in oxidation behavior between AM and CM alloy IN625, elucidate the mechanism of IGO in AM Ni-base alloys and suggest potential mitigation strategies against IGO in AM high-temperature metallic materials. The AM IN625 alloy batch studied in [12,13] was compared with the CM IN625 alloy batch from [26] and air oxidation exposures for up to 1000 h at 900 °C were performed. The oxide scales were characterized with scanning electron microscopy (SEM), energy dispersive X-ray analysis (EDX), electron backscatter diffraction (EBSD), transmission electron microscopy (TEM) and atom probe tomography (APT).

EXPERIMENTAL

Materials

Cubes of AM IN625 measuring 15 x 15 x 15 mm³ were manufactured by Powder Bed Fusion – Laser Beam (PBF-LB) and provided by Siemens Energy AB (Finspång, Sweden) in the as-built condition. To analyze the microstructural anisotropy of the obtained AM material, the AM IN625 cubes were sectioned in two directions: parallel (AM-X and AM-Y) and perpendicular (AM-Z) to the build axis, as visualized e.g. in [12]. As no differences between the longitudinal X and Y cuts were detected, both parallel to the build direction, hereinafter only AM-Y is compared vs. the transversal AM-Z cut.

The CM alloy IN625 was a forged bar supplied by Huntington Alloy Corp (New York, USA). The same CM alloy batch was studied in [26]. The chemical compositions of AM and CM IN625 obtained by ICP-OES are given in **Table 1**.

The alloy coupons of AM IN625 were machined to 15 x 15 x 2 mm³ dimensions. One AM IN625 cube was hot-rolled by HMW Hauner GmbH (Röttenbach, Germany). The as-built

AM alloy cube was heated to 980 °C and rolled to a 2.5 mm thick sheet. The alloy coupons of AM IN625 were machined either to 15 x 15 x 2 mm³ for furnace exposures or 20 x 10 x 2 mm³ for experiments in a thermobalance. The surfaces were ground with SiC papers and polished to 0.25 µm with diamond pastes.

Thermobalance exposures

The *in-situ* oxidation kinetics measurements were isothermally performed with a SETARAM thermobalance in flowing synthetic air for up to 72 hours at 900 °C. The heating rate was 90 K min⁻¹ and the cooling rate was 10 K min⁻¹.

Long-term air exposures

Isothermal exposures were performed in tube furnaces (\varnothing 44 mm) at 900 °C in stagnant lab air for up to 1000 h. The specimens were degreased in ethanol and acetone prior to exposure and directly introduced into the hot zone of the tube furnace. The temperature calibration was performed by an external Pt/Rh-thermocouple placed next to the specimens. After exposures, the specimens were removed from the hot zone of the furnace and cooled down in air. The mass gain curves were obtained by gravimetric measurements prior and after the exposures using Mettler Toledo XP6 microbalance with a 1 µg resolution.

Electron microscopy

Electron backscatter diffraction (EBSD) maps were obtained on the oxidized specimens using a Zeiss Merlin scanning electron microscope (SEM) equipped with a mounted Nordlys Elec-tron backscattered diffraction (EBSD) system (Oxford Instruments, UK). An FEI Quanta 200 SEM equipped with an Oxford X-max 80 energy dispersive X-ray (EDX) spectrometer was employed for pre- and post-exposure analysis. Aztec software was

used to evaluate the EDS data. Cross-sections were made on exposed samples by the broad-ion beam (BIB) technique using a Leica EM TIC 3X, as well as by conventional polishing with diamond pastes ($0.25\text{ }\mu\text{m}$) and colloidal silica ($\approx 50\text{ nm}$) after hot mounting into Bakelite. The specimens were gold sputtered and electroplated with nickel prior to hot mounting.

GD-OES

GD-OES (Glow Discharge Optical Emission Spectrometry) concentration profiles were obtained using a Horiba Jobin Yvon spectrometer (Palaiseau, France). The GD-OES depth profiles were quantified following the procedure described in [27–29].

Focused Ion Beam/Scanning Electron Microscopy, FIB/SEM

An FEI Versa 3D combined Focused Ion Beam/SEM (FIB/SEM) workstation was used to produce cross-section thin-foils from the oxide scale and subjacent metal. In order to protect the oxidized surface during the subsequent ion milling, a thin Pt layer ($25 \times 5\text{ }\mu\text{m}^2$) was first deposited on the surface using Electron-Beam Induced Deposition (EBID) from a Pt-containing precursor gas. Then a thicker Pt layer (with a thickness of $\sim 2\text{ }\mu\text{m}$) was deposited on top using Ga Ion-Beam Induced Deposition (IBID). At the initial stages of the milling, higher ion currents were used, while lower currents were chosen at the final stages to produce finer milled surfaces. Lower ion energies (2 and 5 kV with ion currents of 49 and 27 nA, respectively) were selected in the final stages of polishing to minimize the potential artefacts from FIB milling.

Scanning Transmission Electron Microscopy, STEM

Scanning Transmission Electron Microscopy (STEM) was performed using an FEI Titan 80-300 TEM/STEM equipped with an Oxford Instruments EDX detector and a Field Emission Gun (FEG) to acquire STEM micrographs in High Angle Annular Dark Field

(HAADF) and Bright Field (BF) modes, as well as to obtain chemical composition and EDX concentration maps.

Atom Probe Tomography, APT

The FEI Versa 3D dual-beam FIB–SEM workstation was also used to prepare samples for atom probe tomography (APT). A well-established *in situ* lift-out specimen preparation was employed as in [30]. The atom probe measurements were performed using a local electrode atom probe CAMECA LEAP 6000 XR. The instrument was used in laser pulse mode at 40 K specimen temperature, 0.5–1.0 % evaporation rate, and 50 pJ laser pulse energy. Auto pulse frequency control was implemented and set to guarantee a minimum mass spectrum range of 180 Da. CAMECA APT Suite 6 reconstruction software was used to analyze the obtained APT data.

RESULTS

Thermogravimetry, TG

Figure 1 shows the in-situ recorded oxygen uptake by alloy IN625: as-printed AM (Y- and Z-cuts), AM alloy after hot-rolling and CM alloy during exposure in synthetic air at 900 °C. All AM variants of the alloy demonstrated a higher oxidation rate compared to CM. The oxidation kinetics for CM is parabolic and agrees well with the literature TG data for alloy IN625 [15,31]. The parabolic rate constants in terms of oxide thickness assuming an exclusive formation of Cr₂O₃ were calculated from the curves in **Figure 1** and summarized in **Table 2**.

The AM alloys demonstrated a weak oxidation rate anisotropy, i.e., the mass change recorded for the Z-cut specimen was slightly higher than that for the Y-cut specimen. The oxidation rate for the hot-rolled specimen (AM-HR) was even higher than those of AM-Y

and AM-Z. A clear correlation between the GB density and the oxidation rate can be concluded from the TG-curves, i.e., the higher the GB density (AM-HR > AM-Z > AM-Y), the higher the oxidation rate.

Figure 2 demonstrates the long-term oxidation kinetics measured for AM-Y, AM-Z, AM-HR and CM during a discontinuous air exposure at 900 °C for up to 1000 h. The AM alloy specimens, as well as AM-HR, oxidize faster than CM in agreement with the TG-curves in **Figure 1**. Unlike the short-term *in-situ* measurements in **Figure 1**, the oxidation kinetics over 1000 h is sub-parabolic and can be well approximated, e.g., with a cubic time law demonstrating that the oxidation rate gradually decreases with time.

No significant differences were found between the transversal (AM-Z) and the longitudinal (AM-Y) sections of the AM specimen. Hot-rolling had a minimal effect on the overall long-term oxidation kinetics. No signs of oxide spallation and mass loss over 1000 h exposure were detected.

Oxide scale morphology

Figure 3 illustrates the temporal evolution of the oxide scale morphologies on AM-Y, AM-Z, AM-HR and CM alloy IN625. The intermetallic phase δ -Ni₃Nb is precipitated at the oxide metal interface in all specimens, which is a common feature for alloy IN625 [26]. The AM alloy specimens develop a distinctive oxide scale morphology upon oxidation, as reported in our previous publications [12,13] as well as in literature [9–11,16,17].

The Cr₂O₃ scale grown on AM IN625 is prone to buckling. This occurs primarily above the alloy GBs and is already observable after 24 h. A hollow void forms underneath the buckled oxide. After longer oxidation times, the void is filled with newly grown Cr₂O₃ and appears as a compact ridge in the cross-section after longer exposure times. The oxide ridge is accompanied by a network of elongated intergranular voids along the alloy GBs. After even longer oxidation times, these voids are often filled with Cr₂O₃ and Al₂O₃ [12].

The hot-rolled AM alloy specimens demonstrated virtually the same oxide scale morphology as the as-printed AM material, i.e., the buckled Cr₂O₃ scale is accompanied by subscale porosity. The pattern of this porosity differed from AM-Y and AM-Z due to a

smaller grain size, e.g., the IG voids do not appear elongated in AM-HR. At the same time, the void depth is similar to that in AM-Y and AM-Z while the voids in the outer part, close to the oxide-metal interface, are filled with oxide already after 168 h of oxidation.

Finally, the CM specimens reveal a totally different oxidation pattern compared to the AM specimens. The external Cr_2O_3 scale appears corrugated, i.e., growing under compressive stresses. However, no signs of a massive oxide decohesion as in the AM specimens have been detected in any CM specimens up to 1000 h. Sporadic oxide decohesion was observed only after 24 h (see the CM column in [Figure 3](#)), which did not develop further into oxide ridges after longer exposure. The CM alloy IN625 demonstrated a characteristic oxide scale morphology revealing all well-documented phenomena such as:

- i) dissolution of $\delta\text{-Ni}_3\text{Nb}$ and its re-precipitation at the oxide-metal interface
- ii) dissolution of M_6C carbide (not present in the microstructure of AM due to the lower C content, see [Table 1](#))
- iii) coarsening of the alloy grains in the subsurface precipitate-free zone
- iv) internal precipitation of Al_2O_3 at the alloy GBs underneath the Cr_2O_3 scale

The SEM back-scattered electron (BSE) images in [Figure 4](#) show the oxide scales grown on the CM ([Figure 4a](#)), AM ([Figure 4b,d](#)) and hot-rolled AM ([Figure 4c](#)) specimens after 1000 h air oxidation at 900 °C. After this exposure, the Cr_2O_3 scale grown on the CM specimen is morphologically very similar to the scales observed at shorter exposure times ([Figure 3](#)). On the AM alloy specimens, thick and pronounced oxide ridges can be seen above the GBs in the alloy ([Figure 4b,d](#)). Apart from the elongated voids at the metal GBs, spherical voids are present within the grains in the oxidation affected zone. No in-grain voids were detected in AM-HR. Presumably because of the small grain size in AM-HR, the voids tended to condense at the GBs. Additionally, the oxide ridges formed on AM-HR merge into a continuous layer of Cr_2O_3 that appears thicker in the BSE images compared to the AM-Y and AM-Z specimens due to a higher GB density in hot-rolled AM. An unwrinkled section of the Cr_2O_3 scale can be seen in the right-hand part of [Figure 4c](#).

EBSD maps in [Figure 5](#) illustrate the grain structure of the Cr_2O_3 scales shown in [Figure 4](#). On all four alloy specimens, the Cr_2O_3 scales reveal a grain size distribution typical for

air grown Cr_2O_3 , i.e., smaller Cr_2O_3 grains are visible at the oxide-metal interface while the larger Cr_2O_3 grains are in the outer part of the scale.

In the AM specimens (**Figure 5b-d**), small grains of the newly formed Cr_2O_3 are present at the base of the oxide ridges in the immediate vicinity of the oxide-metal interface and the corresponding GBs.

Kernel average misorientation (KAM) maps presented in **Figure 6** allow to qualitatively estimate dislocation densities in CM and AM IN625 specimens after 1000 h of air exposure at 900 °C. An increased KAM value (light green signals on the dark blue background) is indicative of a locally increased dislocation density. In CM, the KAM values are increased only in the internal oxidation zone of Al, i.e., at the alloy GBs where Al_2O_3 precipitated. The AM specimens reveal an extensive network of lattice misorientations in the entire material, which is common for AM alloys [32]. Interestingly, hot-rolling and the following recrystallization did not completely remove lattice misorientation in the alloy (see **Figure 6c**).

Figure 7 shows EDX elemental maps for AM, AM-HR and CM alloy IN625. The EDX maps of Nb and Mo illustrate the dissolution/re-precipitation process of the $\delta\text{-Ni}_3\text{Nb}$ phase in all versions of alloy IN625. The elongated voids underneath the oxide scale in the AM specimens contain oxides, both Cr and Al being present in the voids. In other words, the AM alloy specimens suffered from IGO.

Transport parameters

Figure 8 displays the kinetics of the Cr_2O_3 scale growth in terms of oxide thickness for AM, AM-HR and CM alloy IN625 during air oxidation for up to 1000 h at 900 °C. The thickness of the smooth, unwrinkled scales was measured in the SEM BSE images. The oxide thickness growth kinetics is parabolic, $k_p^{\text{Cr}_2\text{O}_3} = 5.5 \times 10^{-18} \text{ m}^2\text{s}^{-1}$, and matches well the parabolic constant available in literature, $k_p^{\text{Cr}_2\text{O}_3} = 8 \times 10^{-18} \text{ m}^2\text{s}^{-1}$ [26]. The parabolic constants were calculated using the following expression:

$$X_{\text{Cr}_2\text{O}_3}^2 = 2k_p^{\text{Cr}_2\text{O}_3}t \quad (1)$$

here $X_{Cr_2O_3}$ is oxide thickness in m, t is exposure time in s.

Remarkably, the growth rate of the unwrinkled Cr_2O_3 scale is not sensitive to the metallurgical state of the alloy, i.e., AM, AM-HR or CM.

Figure 9 shows Cr depth concentration profiles measured with SEM EDX in CM, AM and AM-HR alloy IN625. The experimental measurements (symbols) are compared with the calculated Cr-profiles (lines) computed using the Wagnerian depletion model [33] as described e.g. in [34].

According to the classical selective oxidation model [33], the parabolic rate constant $k_p^{Cr_2O_3}$ and Cr interdiffusion coefficient \tilde{D}_{Cr}^{alloy} (in m^2s^{-1}) are related to the Cr depletion at the oxide metal interface, i.e., the difference between the initial Cr concentration in the alloy, C_{Cr}^{bulk} in wt. %, and the time-independent Cr-interface concentration, C_{Cr}^{int} in wt. %, by the following expression:

$$C_{Cr}^{bulk} - C_{Cr}^{int} = \frac{M_{Cr}}{M_{alloy}PBR} \frac{100}{\left(\frac{\pi k_p^{Cr_2O_3}}{2\tilde{D}_{Cr}^{alloy}} \right)^{\frac{1}{2}}} \quad (2)$$

here $M_{Cr} = 52.0$ molar mass of Cr, $M_{alloy} = 57.1$ averaged molar mass of the alloy, PBR is Pilling-Bedworth ratio, i.e., the ratio of the formed oxide molar volume to the consumed metal molar volume. For Cr_2O_3/Cr , $PBR = 2.1$.

The experimental values of $k_p^{Cr_2O_3}$ calculated with Eqn. (1) as well as the calculated \tilde{D}_{Cr}^{alloy} values using Eqn. (2), are summarized in **Table 2**. An averaged $k_p^{Cr_2O_3}$ value of 1.0×10^{-17} determined from the long-term experiment was used for the Wagnerian calculation.

For CM alloy IN625 (**Figure 9a**), the measured Cr depletion profiles are in very good agreement with the calculation, as well as with the previously published data [26]. The parabolic constant k_p employed in the calculation is identical to the experimental fit parameter in **Figure 8**. The interface Cr concentration in CM is 15 ± 0.3 wt.%, as reported for this alloy batch exposed in air at 900 °C [26].

Remarkably, the interface Cr concentration in the AM specimens is also close to 15 wt.% (**Figure 9b**) despite the higher oxygen uptake (see **Figure 1** and **Figure 2**) and, thus, a

higher Cr consumption rate. This may indicate faster Cr diffusion in the AM alloy compensating for the enhanced Cr removal from the alloy. Indeed, the Cr depletion depth after 1000 h oxidation at 900 °C in CM (**Figure 9a**) is 80 µm while that for AM increased to 140 µm (**Figure 9b**). This acceleration of both Cr consumption and supply is reflected in both respective kinetic parameters, k_p and \tilde{D}_{Cr}^{AM} , increased by a factor of 2 (see **Table 2**). The Cr-depletion profiles in the AM alloy are very similar for both the longitudinal (Y-cut) and transversal (Z-cut) sections, i.e., no anisotropy of Cr diffusion was detected.

Finally, the measured Cr depletion profiles in AM-HR (**Figure 9c**) were in good agreement with the profiles calculated for AM Y and Z cuts implying that hot-rolling and, hence, the grain size in the AM alloys studied had a limited effect on the overall Cr transport. In other words, the experimental Cr depletion profiles in the hot-rolled AM alloy were well fitted with the kinetic parameters for AM.

Figure 10 presents the temporal evolution of the void depth in AM and AM-HR alloy IN625 during air oxidation at 900 °C. The void propagation kinetics is diffusion-controlled and parabolic, the parabolic rate being $k_p^{void} = 3.5 \times 10^{-16} \text{ m}^2\text{s}^{-1}$, which is close to the Cr interdiffusion coefficient in IN625 (**Table 2**).

Minor elements

Figure 11 presents GD-OES profiles of the minor alloying elements with a high affinity to oxygen, i.e., Al, Si, Mn and Ti. These elements are commonly found in high-temperature alloys for melt deoxidation and impurity (e.g. S, N) gettering purpose and have different explicit effects on oxidation behavior of NiCr-base alloys [35].

The Al profiles (**Figure 11a**) demonstrate an enrichment zone beneath the Cr_2O_3 scale, which is well correlated with the internal oxidation zone of Al (**Figure 7**). Al_2O_3 is precipitated at the GBs in CM and in the subsurface voids in the AM specimens. In contrast to the profiles of Si, Mn and Ti, the Al profile shape is sensitive to the alloy

microstructure, primarily the grain size indicated by the difference between AM-HR and the two samples AM-Y and AM-Z.

The Si depth profiles (**Figure 11b**) of all AM specimens are uniform, suggesting that no precipitation of SiO_2 occurs at the alloy GBs. The most striking difference between AM and CM is a distinct Si peak underneath the Cr_2O_3 scale and the overall higher Si content in CM, as previously discussed [13].

The concentration profiles of Mn (**Figure 11c**) demonstrate a continuous depletion of this element from the alloy and its incorporation into the Cr_2O_3 scale. The highest Mn concentrations are measured at the outer gas-oxide interface. The Mn enrichment in the oxide is more pronounced for CM which has a factor of 2-3 more Mn in the alloy compared to the AM variant (**Table 1**).

The Ti concentration profiles (**Figure 11d**) show that Ti also penetrates the Cr_2O_3 scale and enriches at the upper (gas-oxide) and lower (oxide-metal) interfaces of the scale. The Ti enrichment in the Cr_2O_3 scale is stronger in CM compared to the AM specimens, although the Ti content in both alloys is similar (**Table 1**). Except for Si, the profiles of the minor elements in CM and AM have very similar shapes.

Transmission Electron Microscopy and Atom Probe Tomography, TEM and APT

Figure 12 displays BF and HAADF TEM images of the Cr_2O_3 scale thermally grown on AM-Y after 24 h in air at 900 °C. The oxide scale is $1.2 \pm 0.3 \mu\text{m}$ thick. The average grain size of Cr_2O_3 in the outer part of the scale is approximately 300 nm, decreasing to tens of nm towards the bottom of the scale. The scale contains small (10-30 nm) bright inclusions in its middle part, down to the metal-oxide interface.

Figure 13 shows BF and HAADF TEM images of the Cr_2O_3 scale grown on CM after 24 h in air at 900 °C. The Cr_2O_3 scale on CM is microstructurally very similar to that on the AM specimen (**Figure 12**), with the same thickness. Larger grains (200 - 300 nm) are visible in the outer part of the scale, while smaller ones (50-100 nm) are found in the

vicinity of the oxide-metal interface. Again, small bright particles are seen in the HAADF image. The nature of these inclusions will be discussed in the second part of this study to be published separately. Some pores can be found (dark in HAADF) inside the scale, especially at the metal/oxide interface, where a linkage of pores can be observed.

A summary of the APT results for chromia, with the tip direction parallel to the oxide/metal interface, obtained on AM-Y and CM after 1000 h at 900 °C, is presented in [Figure 14](#) and [Figure 15](#), respectively. The two oxide scales differ locally in grain size: multiple grains and GBs are visible for the AM scale, while a single GB is crossed in the APT run of the CM oxide. This matches the findings shown by the EBSD mapping above ([Figure 5](#)). GBs are highlighted by substantial segregation of elements, as demonstrated by the 1D concentration profiles plotted in [Figure 14b](#) and [Figure 15b](#). Ti is the main segregating element and can reach concentrations of 8–10 at. % at the GBs. Other segregating elements are Nb, Si and Al. The chemistry of GBs found in AM and CM scales is close to identical. Ni is not found at the GBs, but it forms Ni-rich particles distributed throughout the oxide matrix in the AM chromia ([Figure 12](#)). A weak tendency for the same phenomenon is visible in the CM case, where Mn-rich particles are predominantly found instead. As shown by GD-OES, the Mn concentration in the oxide is higher in CM. The APT data show that Mn is repelled from the GB-zone and enriches in the regions distant from it, where substantial presence of small Mn-rich precipitates is present. Another element displaying an interesting segregation pattern is Al. Similarly to Mn, Al enriches preferentially in certain regions of the oxide matrix. The Al-rich and Mn-rich zones do not overlap in the CM oxide. The differences in oxide matrix composition between AM and CM has presumably a kinetic nature [36,37]. Once a Cr₂O₃ grain is nucleated, it sporadically encloses a certain amount of the accompanying minor elements from the alloy such as Mn and Al. At 900 °C, bulk diffusion in Cr₂O₃ is too slow to homogenize the concentration gradients of these elements between different grains, which is the most plausible explanation of the elemental distribution in the studied chromia scales. The chemical differences within one oxide grain are fascinating and deserve further studies which are outside the scope of this paper.

Figure 16 illustrates the sampling and APT reconstructions from a single needle specimen extracted at the oxide-metal interface in the CM IN625 specimen exposed in air for 1000 h at 900 °C. Fig. (a) shows the position from which the needle specimen depicted in Fig. (b) was extracted. Fig. (b) displays images from intermediate steps in the annular milling clearly showing the different phases (oxide-metal-oxide). A 10 nm slice of the reconstruction from the measurement of phase boundary I (PB I) displaying O and Ni ions is shown in Fig. (c). In addition, 2 nm slices viewed perpendicular to the oxide-metal interface are displayed, which show that an approximately 20 nm thick layer in the oxide at the interface is enriched in Ti and Al. The same specimen was re-sharpened after the first APT measurement. Fig. (d) shows the reconstruction of the second measurement capturing the interface in the opposite sequence (PB II), i.e., from the metal into the oxide. The concentration profiles in Figs. (e), (f) and (g), (h) are from the reconstructions in Figs. (c) and (d), respectively. Both cases exhibit an approximately 20 nm thick layer of oxide that contains ~ 2 at% Ti and ~1 at% Al. The fact that the Ti- and Al-rich layer is shown in both cases, i.e., the oxide-to-metal and metal-to-oxide sequence, rules out APT related artifacts that can affect measurements when the analysis direction is from the oxide into the metal [38,39]. This segregation of Ti and Al at the oxide-metal interface is also observed on the microlevel in the GD-OES profiles (**Figure 11**). Remarkably, Si was not detected immediately at the oxide-metal interface (compare e.g. with **Figure 11b**) suggesting that SiO_2 is presumably precipitated as individual precipitates as reported for a Cr_2O_3 forming model alloy $\text{FeCr}(\text{NbTiSi})$ [36].

In Figs. (e) and (f), it is shown that this layer additionally has a gradient in Cr and O concentration, indicating the presence of a phase other than chromia at the oxide-metal interface before reaching the constant Cr : O ratio (right hand side in Fig. (e)). The underestimation of O in chromia (~ 52 at. % instead of the nominal 60 at. %) it has been reported recently [40], hence we are confident that despite the lower apparent O concentration the oxide is chromia Cr_2O_3 .

DISCUSSION

Oxidation kinetics

The kinetics of alloy IN625 air oxidation at 900 °C is well documented in literature [12,15,16,26,31,41]: both for CM [15,26,31,41] and more recently for AM [12,15,16,26,31]. Some of the afore-mentioned studies report *in-situ* TG-curves [15,26], while most studies present discontinuous or isothermal long-term oxidation data [12,16,26,41]. The $k_p^{Cr_2O_3}$ values calculated in terms of oxide thickness in $m^2 s^{-1}$ using Eqn. (1) are summarized in **Table 3**. Only data for oxidation of CM alloy IN625 in dry air at 900 °C were considered. The experimental $k_p^{Cr_2O_3}$ values obtained in the present study agree very well with those reported in literature. It is remarkable that the $k_p^{Cr_2O_3}$ values for the short-term *in-situ* experiments, both ours and the literature data, are systematically higher by a factor of 1.5 than the rate constants derived from long-term exposures. Furthermore, the short-term data are much better fitted with the parabolic time law than the long-term data. This implies that oxidation kinetics of alloy IN625 is sub-parabolic, i.e., it tends to decelerate after longer exposure times. Sub-parabolic kinetics is more common for α -Al₂O₃-scales in which transport is limited by inward diffusion of oxygen via oxide GBs. As the Al₂O₃ grains in the bottom part of the oxide scale continue to grow, the GB density decreases leading to a deceleration of oxide growth as demonstrated in [42]. A similar microstructural pattern was observed in the Cr₂O₃ thermally grown on alloy IN625 (**Figure 5**, **Figure 12**, **Figure 13**), which is further discussed in the next section.

Interpretation of the directly measured $k_p^{Cr_2O_3}$ values for the AM specimens (see **Table 2**) is difficult. First, the $k_p^{Cr_2O_3}$ values are higher by a factor of 2 than $k_p^{Cr_2O_3}$ for CM, both short-term and long-term, due to intergranular oxidation. A mass-balance calculation in [12] showed that the oxygen uptake by IGO, i.e., oxide ridges and oxide in the voids, may amount to 50%, which implies a factor 2 increase of the gravimetric $k_p^{Cr_2O_3}$ and agrees well with the experimental values (**Table 2**). However, it is impossible to single out these IGO contributions based only on the TG data.

Cr₂O₃ scales

The oxidation behaviour of alloy IN625 at 700-1000 °C is well-studied highlighting the oxidation kinetics [26,43,44], the oxidation-driven phase transformations [26,45], as well as the transition to unprotective behaviour, i.e. formation of NiO [43,44,46]. At the same time, there is hardly any high-resolution microstructural analysis of the Cr₂O₃ scales thermally grown on IN625.

The oxide grain size distribution in the Cr₂O₃ scales grown on all alloy IN625 specimens in this study, i.e., CM, AM or AM-HR, is systematically reproduced irrespective of the substrate microstructure. The grain size increases towards the outer gas-oxide interface (**Figure 5**, **Figure 12**, **Figure 13**). Such microstructures of the Cr₂O₃ scales, reported mainly for NiCr-base binary model alloys [47,48], are typical for Cr₂O₃ scales grown in high-pO₂ environments and indicate outward growth by Cr cation transport over the oxide GBs. It is evident that neither alloy microstructure (large grains in AM vs. small grains in CM and AM-HR) nor the manufacturing route (AM vs. CM) affect the oxide grain size distribution pattern in the thermally grown Cr₂O₃ scales on IN625.

The chemistry of the GBs in these Cr₂O₃ scales is fascinating in its complexity. As can be seen in the APT reconstructions in **Figure 14**, **Figure 15**, **Figure 16**, virtually all elements from the alloy segregate to the GBs of Cr₂O₃. Especially strong is the segregation of Ti detected within the Cr₂O₃ scale, as well as at the oxide-metal interface. Such a strong segregation of Ti in the Cr₂O₃ scales has been reported for Cr₂O₃ grown on ferritic steels [36,37,49] and a γ-NiCrAl-base alloy [50]. Other elements with a high affinity to oxygen, such as Al, Si, Mn also tend to segregate to the GBs of Cr₂O₃. At the same time, no significant difference in measurable segregations of the alloy constituents to the GBs of Cr₂O₃ can be established between CM and AM. In other words, neither AM manufacturing nor minor differences in alloy compositions had a significant effect on the GB chemistry of the thermally grown Cr₂O₃ on alloy IN625, which is essential for the growth mechanism.

and growth rate of the Cr₂O₃ layer (apart from areas with ridges) and is reflected in the metallographically measured oxide scaling kinetics (see **Figure 8**).

To summarize, the microstructural analyses in this study clearly demonstrate that the Cr₂O₃ scales thermally grown on both AM and CM alloy IN625 are chemically (bulk and segregations to the GBs), microstructurally (grain size distribution in the scale) and kinetically (growth rate) virtually identical. Therefore, the trigger of IGO, as well as the origin of the difference in oxidation behavior between CM and AM, should be sought elsewhere.

Cr diffusion in AM

The Cr depletion profiles in **Figure 9** revealed the following important observations: i) no Cr diffusion anisotropy, i.e., no measurable difference between AM-Z and AM-Y; ii) hot-rolling did not significantly affect Cr diffusion (no difference between AM and AM-HR); iii) Cr diffusion is accelerated in AM (\tilde{D}_{Cr}^{AM} higher by a factor of 2 compared to \tilde{D}_{Cr}^{CM}); iv) the measured Cr profiles systematically depart from the calculated ones in all AM specimens after longer exposure times indicating a faster Cr supply to the oxide-metal interface.

Additively manufactured metallic materials are well-known to develop a dense network of dislocations in the alloy microstructure [6,51–53] due to high cooling rates, large thermal gradients and a complicated thermal history during printing. Dislocations in metals provide a short-circuit diffusion path known as dislocation pipe diffusion [54,55]. It is therefore not surprising that Cr diffusion accelerates in the AM versions of alloy IN625. The literature on diffusion in AM alloys is extremely scarce. Only a few studies report Cr depletion profiles in AM Ni-base alloys [56,57] and AISI 316L [58,59]. Flatter Cr profiles in AM alloys compared to CM and, hence, a faster transport of Cr, are generally reported. An overall acceleration by a factor of 2 can be estimated based on the reported Cr depletion profiles [52–55], which agrees well with the findings in the present study (**Table 1**).

Interestingly, hot-rolling of the AM alloy had a limited effect on the Cr depletion pattern, i.e., the Cr interface concentration (15 wt.%), as well as the Cr depletion depth (140 µm after 1000 h at 900 °C) are very close to the corresponding values in AM (compare b and

c in **Figure 9**). A negligible difference between the Cr depletion profiles in AM and AM-HR may indicate a relatively small contribution of GB diffusion in the AM alloy IN625 at 900 °C as Cr diffusion is presumably dominated by dislocation pipe diffusion in the entire bulk of the AM material. The KAM maps in **Figure 6** show that hot-rolling did not eliminate lattice misorientations and thus high dislocation density in the rolled AM alloy. However, this observation needs further research to elucidate the diffusion mechanism in AM Ni-base alloys and properly quantify the lattice, GB and dislocation contributions. For instance, the GB contribution to Cr diffusion in IN625 is reported to be significant in the CM alloy even at 1000 °C [60].

Enhanced Cr diffusion in the AM alloy may have various consequences for the oxidation resistance of the material. Accelerated Cr diffusion generally implies an improved Cr supply to the oxide-metal interface and better resistance to breakaway oxidation and is often intentionally stimulated by cold-work [61] of the surface to promote protective oxidation [61,62]. On the other hand, higher Cr fluxes through the dislocation network will produce a larger flow mismatch for diffusion Cr and counter-diffusion Ni [63,64] resulting in more intense Kirkendall porosity in the Cr depletion-affected zone. The latter is observed in the present study (**Figure 3** and **Figure 10**) and in the literature. Dislocation pipe diffusion in AM alloys resulting in the subscale porosity is an aggravating factor promoting IGO, however, it is hardly its primary trigger.

IGO in AM Ni-base alloys

Additively manufactured Ni-base alloys are known to suffer from IGO [9–14,16,17,21–24], the mechanism of IGO being actively debated in this literature.

Recently, de Leon Nope et al. [11] summarized the most discussed explanations of IGO as follows:

- i) grain boundary misorientation [65,66];
- ii) minor differences in chemical composition of CM and AM [12,13];
- iii) formation of Kirkendall voids [15,22,23].

The authors in [11] suggest that IGO in AM alloys is triggered by the excess of interstitially dissolved oxygen due to atomizing which promotes internal oxidation and initiates IGO.

It is evident that IGO is a complex mechanism which includes phenomena such as i) oxide decohesion over the GBs, ii) re-oxidation of the alloy underneath the buckled oxide leading to formation of oxide ridges, iii) void formation in the alloy subsurface (within the alloy grains as well as at the GBs), iv) oxidation of alloy constituents with a higher affinity for oxygen than Cr, e.g., Mn, Ti (entering the Cr_2O_3 scale), Al, Si (internally precipitating oxides at the GBs or the oxide metal-interface), v) oxidation of open IG voids after eventual oxide cracking and/or spallation.

Figure 17 illustrates the IGO mechanism that we propose based on the observation in the present study. The evolution of IGO at the triple junction of the GB and the oxide-metal interface is unfolding in the following order:

Stage 1. Decohesion. Oxide growth and decohesion over the GBs (**Figure 17a**). A smooth oxide scale forms over the alloy grains, while a segment of the scale above the GB detaches. Simultaneously, voids form along the GBs in the underlying alloy. These IG voids appear in the earliest stages of oxidation, e.g., already after 2 h of exposure as shown in [12].

Stage 2. Oxide buckling (**Figure 17b**) is the second important step in the IGO mechanism. Thermally grown oxide scales grow under compressive stresses because of the higher molar volume of the oxide compared to that of the consumed metal (for Cr_2O_3 on a NiCr-base alloy the Pilling-Bedworth ratio is 2.12) [67,68]. These stresses can be dissipated either through plastic deformation of the metal (relevant for thin components of e.g. ferritic steels [69,70]) or through oxide decohesion, buckling, blistering, and finally oxide spallation. Oxide wrinkling has been observed for Cr_2O_3 formed on Fe-28Cr [71] or even pure Cr [72]. The Cr_2O_3 scales detach and buckle primarily over the alloy GBs where oxide adherence is the weakest and/or metal creep deformation is easier (compare e.g. AM in **Figure 3** with **Figure 17b**). Oxide buckling over the GBs gives rise to large cavities between the oxide scale and the metal. These underlying voids are further filled with the re-grown Cr_2O_3 , as illustrated by finer grains in the newly grown oxide underneath the outer buckled layer in **Figure 5c,d**. Additional Cr consumption to locally re-heal these

voids further intensifies the Cr-depletion and promotes formation and growth of the intergranular (IG) voids. It should be noted that not only IG voids are present in the Cr depleted zones of the AM specimens. Individual spherical voids are also present in the metal (see **Figure 3** and **Figure 4**). However, these voids remain closed and unoxidized (see **Figure 5** and **Figure 7**).

Stage 3. Oxidation. The cavities between the scale and the metal over the GBs open and oxidize (**Figure 17c**). As mentioned above, the growth stresses in the oxide scale can be also relieved through creep and plastic deformation of the alloy. The application of external mechanical loads has been shown to intensify IGO [10] by opening the IG voids and letting them oxidize.

According to this mechanism, IGO in AM alloys is the consequence of two independent, however, overlapping phenomena: a) oxide decohesion and b) intergranular Kirkendall porosity. The latter seems to be an inevitable factor accompanying oxidation of AM alloys. The poorer adherence of Cr_2O_3 to the AM alloy substrate compared to CM thus is the key trigger of IGO. Reasons for oxide decohesion in the case of AM can be listed as follows:

- i) Minor elements. The chemical composition of the AM alloy in the present study (see Mn and Si in **Table 1**) differs slightly from that of the CM batch. The elements with a high affinity to oxygen such as Mn, Ti, Al, Si can be lost due to oxidation during the atomizing process. At the same time, minor precipitations of SiO_2 and Al_2O_3 at the scale-CM-alloy interface may act as pegs and anchors increasing oxide adhesion to the metal [73,74];
- ii) A higher concentration of interstitial oxygen and nitrogen due to the atomizing process may have a similar negative effect on the oxide scale adherence reported for carbon and sulphur in alumina-forming FeCrAl-base alloys [75] although this effect seems to be less relevant for Cr_2O_3 [75];
- iii) Higher densities of dislocations in the AM material, i.e., the main source of IG porosity, may also intensify the vacancy injection at the oxide-metal interface resulting in their condensation and formation of small interfacial voids, poorer adhesion of oxide and decohesion under compressive stresses in the growing oxide [76].

Outlook

The mechanism of IGO proposed in this study, i.e., oxide decohesion and buckling as the main trigger of IGO, was derived by ruling out differences due to AM in the following aspects:

- i) **Cr₂O₃ scale.** No significant differences were found between the scales grown on AM and CM.
- ii) **Subsurface metal.** Cr diffusion in AM is a factor of 2 faster than in CM resulting presumably in Kirkendall porosity in the Cr-depleted zone, however no significant differences were detected otherwise.
- iii) **Metallurgical states.** IGO was observed on various AM specimens irrespective of the microstructural treatment (hot-rolling, annealing, etc.) [12].

The proposed IGO mechanism requires experimental validation and thus further studies. Primarily, batch-to-batch variation needs to be eliminated. In other words, AM and CM alloy versions need to be manufactured from the same alloy batch. This might shed light on the role of the minor alloying elements on oxide adhesion and IGO. It should be borne in mind that AM, to some extent, changes the initial composition of CM introducing interstitials (C,N,O) and possibly binding some minor elements thereby reducing their “free” contents in the alloy matrix. Still, comparing CM with AM produced from the same batch is the best option available to evaluate the impact of the alloy chemistry on high-temperature oxidation of AM alloys.

Alternatively, reactive elements (RE) such as Y, Th or Ce could be introduced into the AM alloy. This would significantly increase oxide adhesion and might prevent the IG voids from opening and oxidation, proving potentially the key role of oxide decohesion in IGO. The mentioned experiments may validate the proposed mechanism and further elucidate the role of AM in the oxidation of high-temperature alloys.

CONCLUSIONS

1. Additively manufactured (AM) Ni-base alloy IN625 oxidizes faster than the conventionally manufactured (CM) alloy during air oxidation at 900°C due to intergranular oxidation (IGO) attack.
2. The AM process does not affect the oxide scale growth mechanism. The Cr_2O_3 scales grown on AM and CM are microstructurally, chemically and kinetically virtually identical.
3. The AM process accelerates Cr diffusion in the alloy. The Cr interdiffusion coefficient in AM is a factor of 2 higher compared to CM at 900 °C. Accelerated diffusion in AM is believed to produce an excessive vacancy flow in the oxidation-affected alloy subsurface producing voids within the grains as well as at the GBs.
4. IGO occurring in AM alloy IN625 is triggered by decohesion of the oxide scale over the GBs. The proposed IGO mechanism consists of three steps.
 - a. The Cr_2O_3 scale detaches from the alloy over the GBs due to compressive growth stresses in the scale and poorer oxide adherence to the AM alloy compared to the CM alloy.
 - b. The oxide scale buckles forming a void between the buckled oxide and the metal. The concurrent Cr-depletion from the alloy gives rise to IG voids due to faster Cr diffusion in the AM alloy compared to the CM alloy.
 - c. The buckled oxide cleaves the IG voids adjacent to the oxide-metal interface, opens them and leads to their oxidation (IGO).
5. Adhesion of Cr_2O_3 to the alloy substrate is thus the key phenomenon triggering IGO in the AM alloy IN625. The difference in adhesion of the Cr_2O_3 scale to the metal substrate between the AM and CM alloys is believed to originate from the differences in chemical composition of the alloys.

Acknowledgements

This study was accomplished within the Swedish High Temperature Corrosion Centre (HTC) partly funded by the Swedish Energy Agency and its member companies (in this work Siemens Energy AB, AB Sandvik Materials Technology, Kanthal AB). The authors also gratefully acknowledge Chalmers Materials Analysis Laboratory (CMAL) where the materials characterizations were carried out. Mr. H. Cosler is acknowledged for performing the TG-experiments. Dr. Anton Chyrkin acknowledges his funding by the European Union, project MSCA4Ukraine, grant No. 1232975. The present publication reflects only the author's views, and the European Union is not liable for any use that may be made of the information contained therein.

CREDIT AUTHORSHIP CONTRIBUTION STATEMENT

Anton Chyrkin: Conceptualization, Investigation, Writing - original draft, Writing - review & editing, Funding acquisition, Project administration.

Andrea Fazi: Investigation, Writing - review & editing.

Mohammad Sattari: Investigation.

David Mayweg: Investigation.

Mattias Thuvander: Writing - review & editing.

Krystyna Stiller: Writing - review & editing.

Mats Halvarsson: Writing - review & editing, Funding acquisition, Project administration,

Wojciech J. Nowak: Investigation.

Egbert Wessel: Investigation.

Dmitry Naumenko: Writing - review & editing.

Jan Froitzheim: Writing - review & editing, Funding acquisition, Project administration.

All authors reviewed the results and approved the final version of the manuscript.

Declaration of Competing Interest

The authors declare that they have no known competing financial interests or personal relationships that could have appeared to influence the work reported in this paper.

Data availability

Data will be made available on a reasonable request.

FIGURES

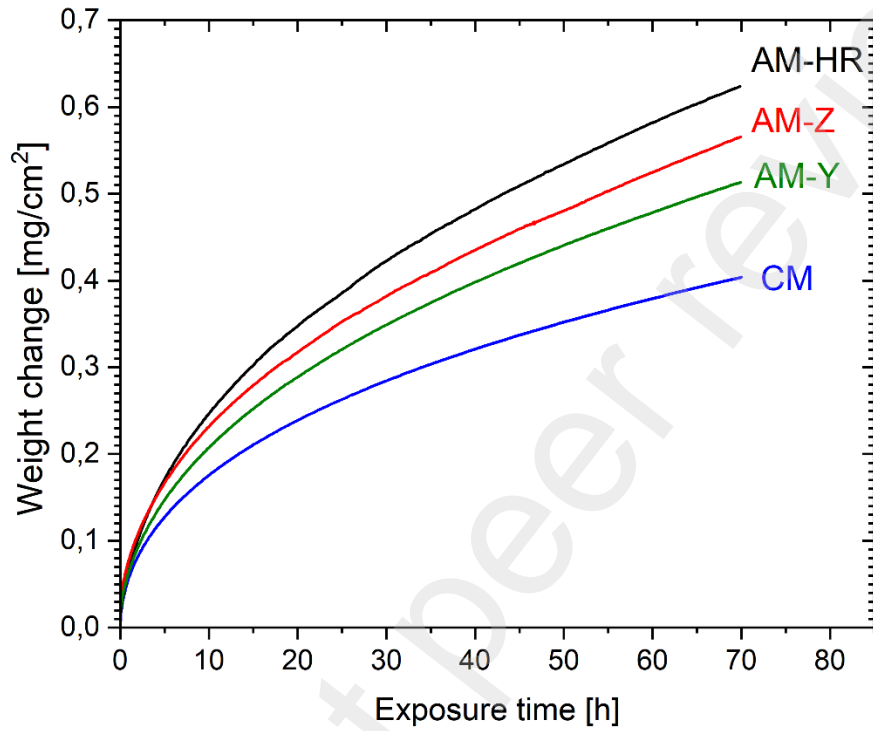


Figure 1: *In-situ* weight change of AM-Y and AM-Z, and hot-rolled AM-HR, together with CM alloy IN625, exposed for 72 hours in synthetic air at 900 °C in thermobalance.

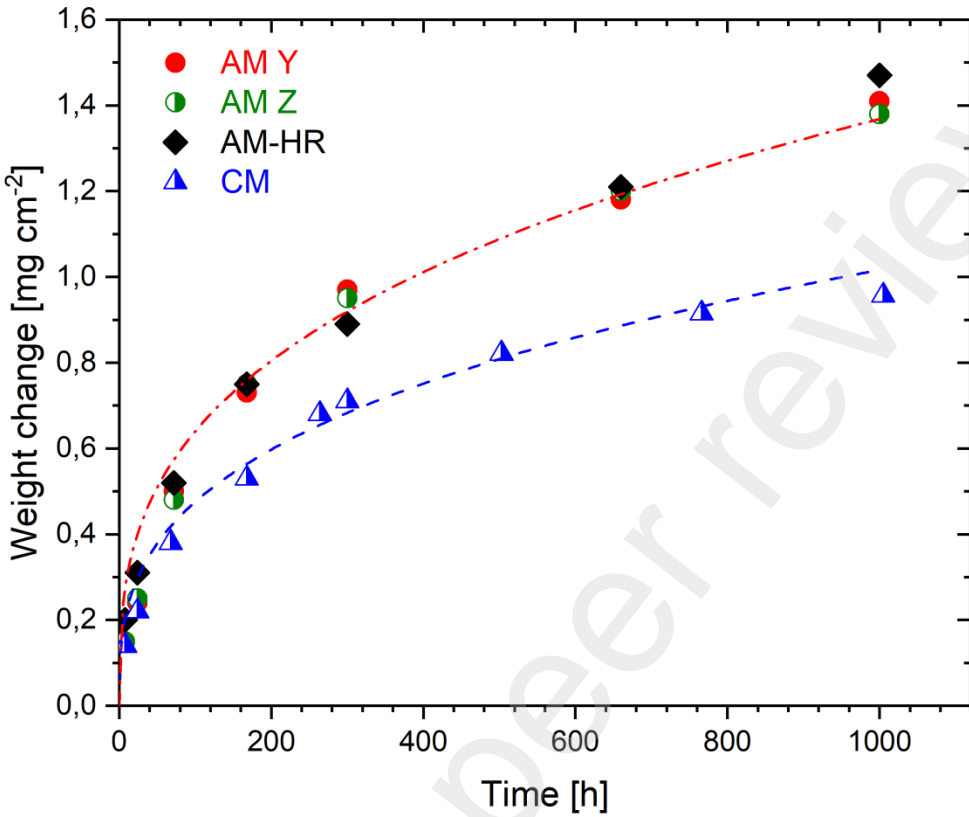


Figure 2: Weight change of the two AM cuts, hot-rolled AM and CM alloy IN625 during discontinuous long-term air exposure at 900 °C. The lines are cubic fit curves $\Delta m = k t^{0.33}$ where $k^{CM} = 0.104$ and $k^{AM} = 0.14 \text{ mg}^2 \text{ cm}^{-4} \text{ s}^{-0.33}$.

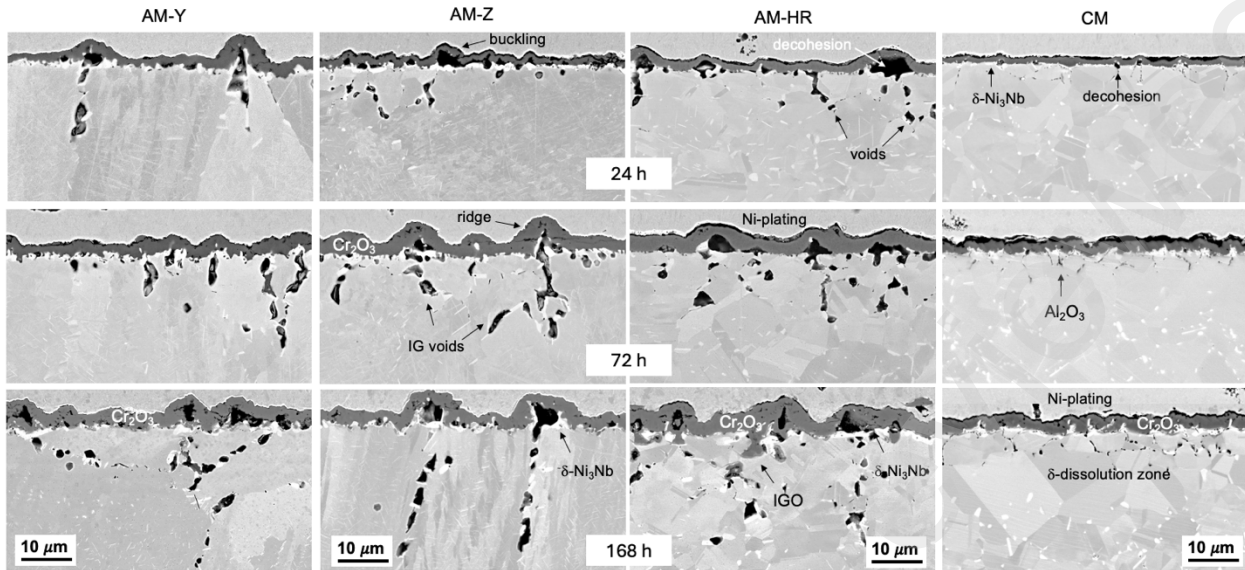


Figure 3: SEM BSE images illustrating the temporal evolution of oxide scales on AM, hot-rolled AM and CM alloy IN625 after 24 h, 72 h, and 168 h air exposure at 900 °C.

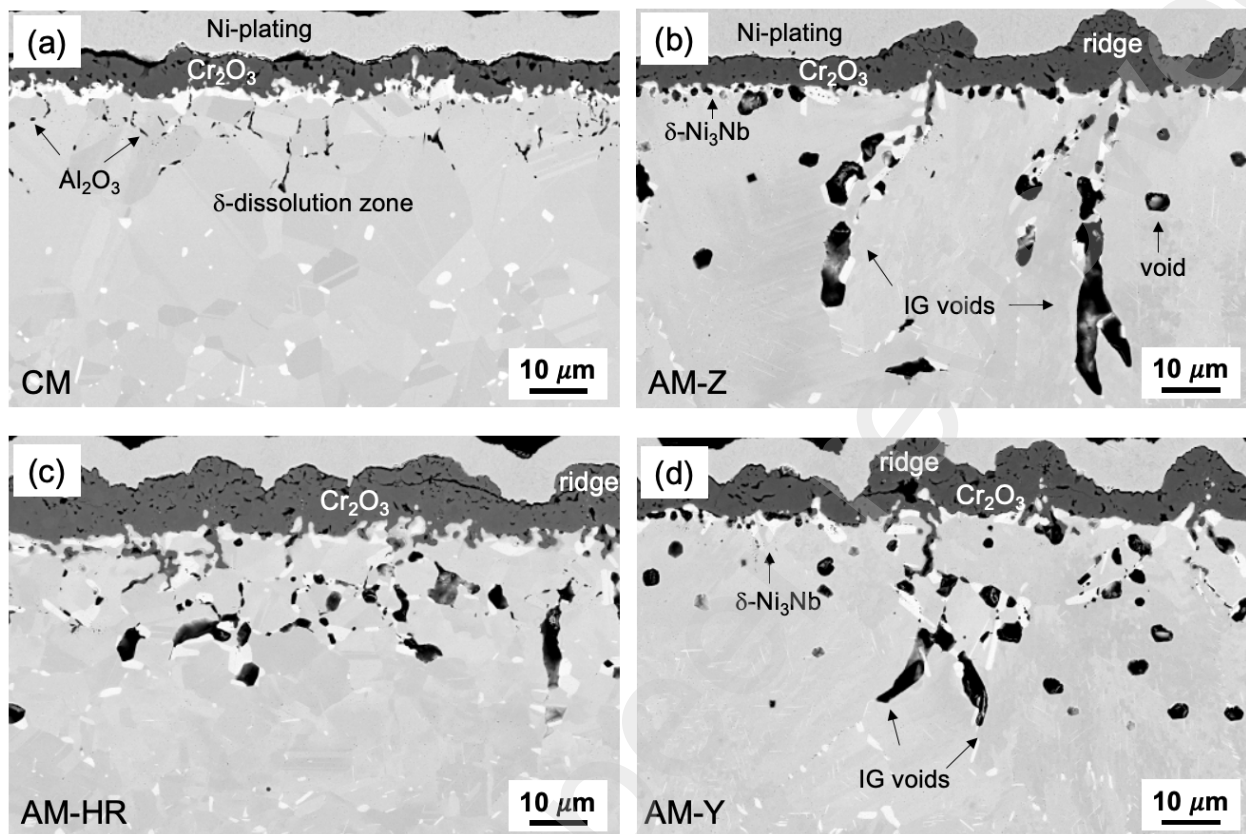


Figure 4: SEM BSE images of oxide scales grown after 1000h air exposure of (a) CM, (b,d) AM and (c) hot-rolled AM alloy IN625 at 900°C.

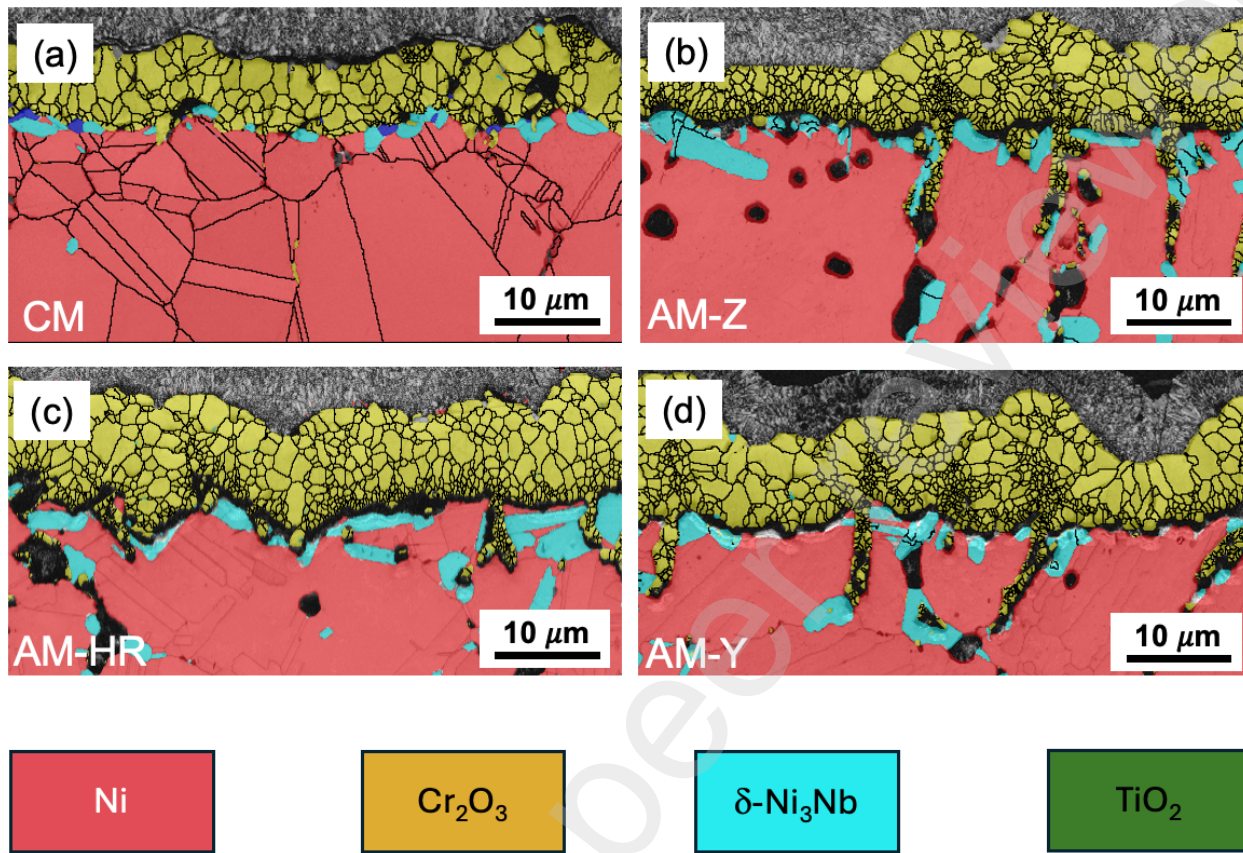


Figure 5: EBSD maps of oxide scales grown after 1000h air exposure of (a) CM, (b,d) AM and (c) hot-rolled AM alloy IN625 at 900°C.

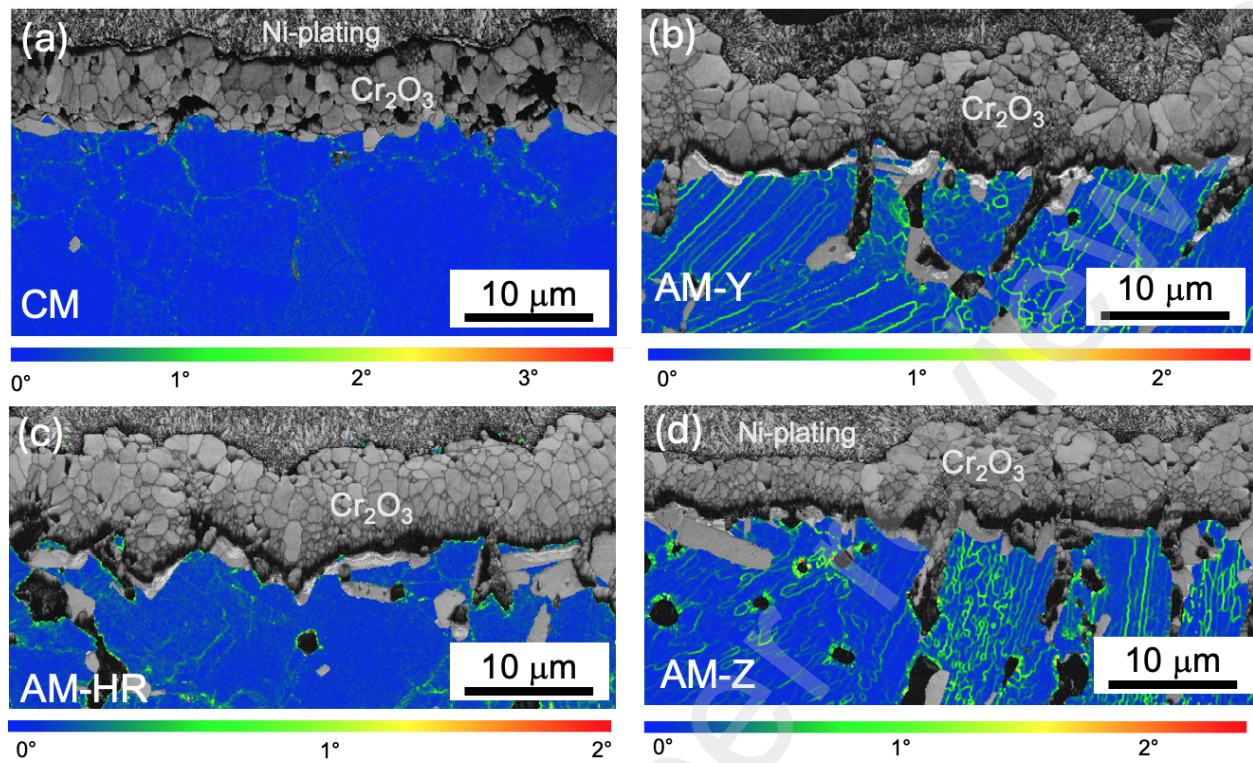


Figure 6: Kernel misorientation maps of oxide scales grown after 1000 h air exposure of (a) CM, (b,d) AM and (c) hot-rolled AM alloy IN625 at 900 °C.

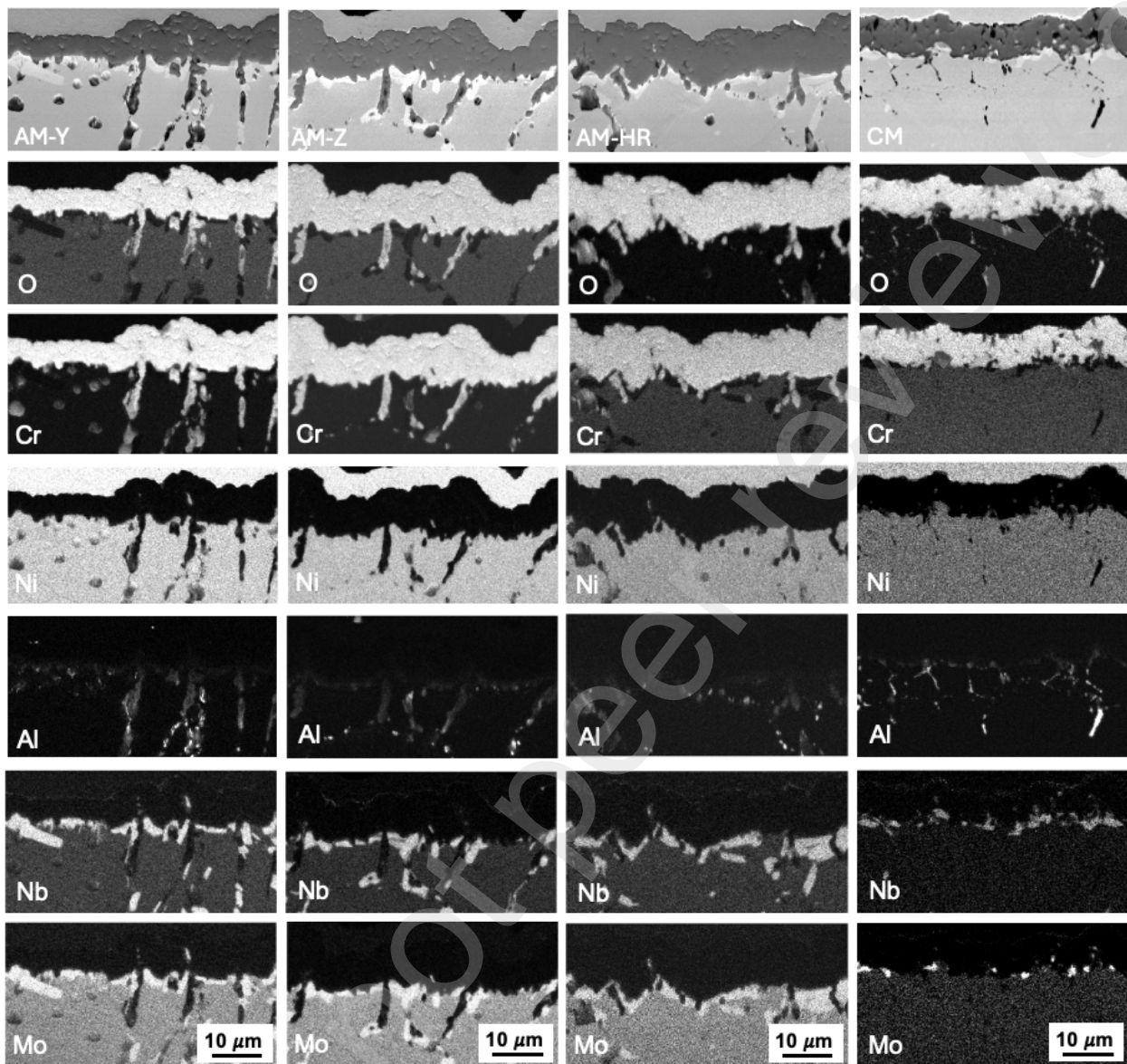


Figure 7: EDX maps of oxide scales grown after 1000 h air exposure of AM, hot-rolled, and CM alloy IN625 at 900°C.

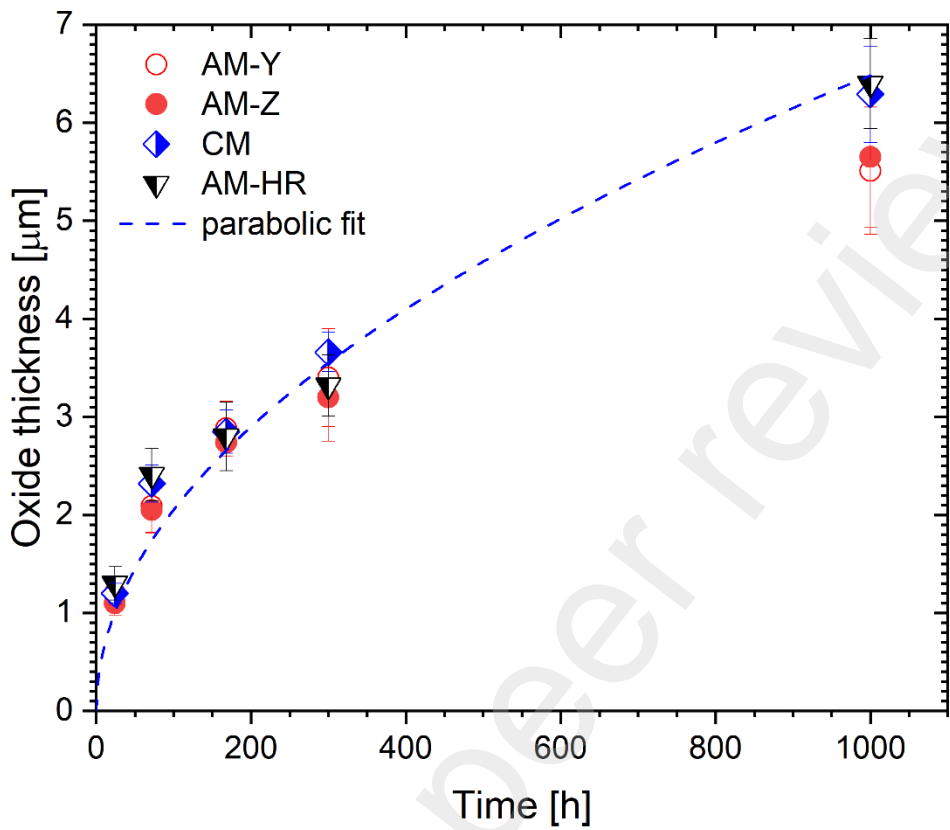
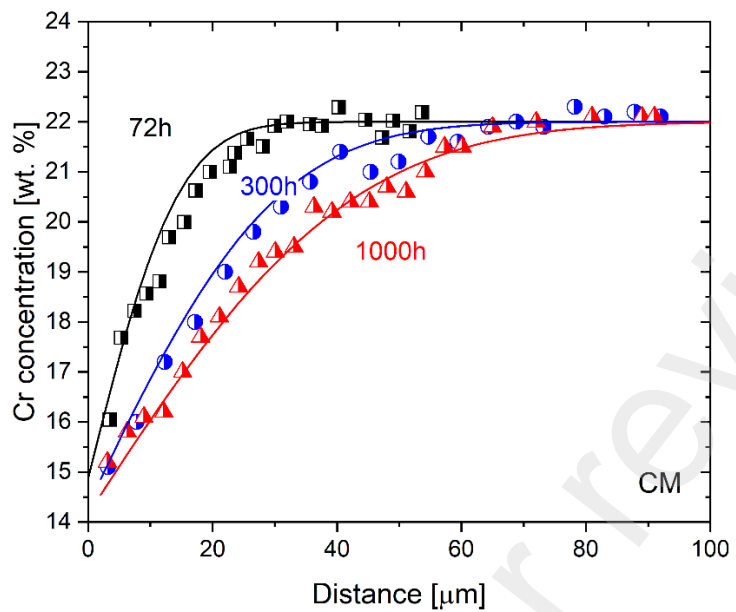
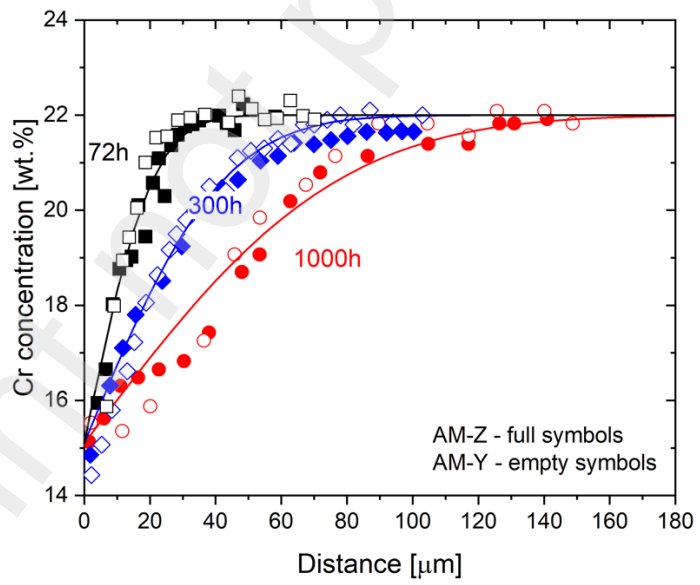


Figure 8: Temporal evolution of smooth Cr_2O_3 scale thickness on flat surface areas of AM, AM hot-rolled and CM alloy IN625 exposed in air at 900°C. Line denotes parabolic fit with $k_p^{\text{Cr}_2\text{O}_3} = 5.5 \times 10^{-18} \text{ m}^2 \text{ s}^{-1}$.



(a)



(b)

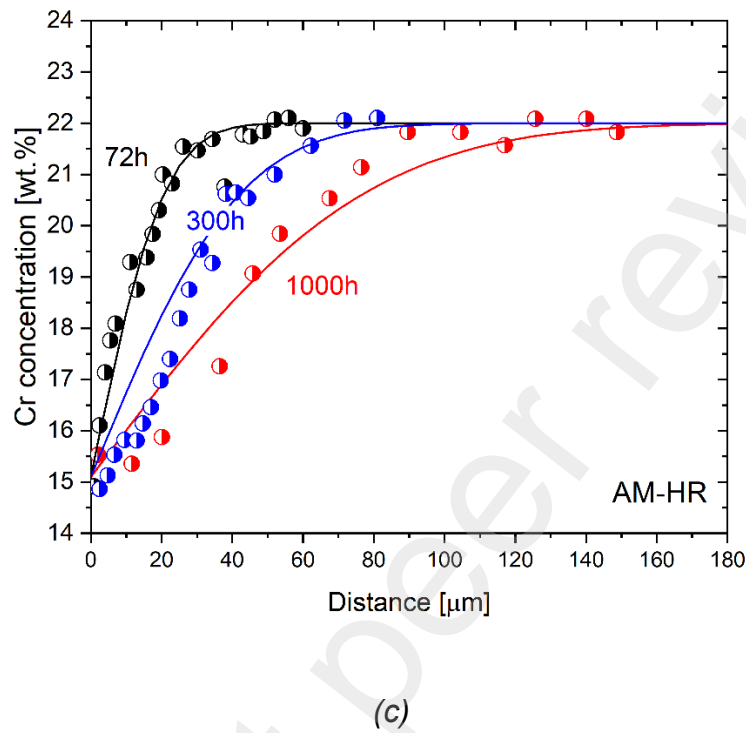


Figure 9: Chromium concentration profiles in CM (a), AM (b) and hot-rolled AM (c) alloy IN 625 after air oxidation at 900 °C measured by SEM EDX (symbols) compared with calculated values (lines) using classical Wagner's theory [33]. The lines were calculated using $k_p = 5.5 \times 10^{-18} \text{ m}^2 \text{ s}^{-1}$, $D_{Cr} = 2.5 \times 10^{-16} \text{ m}^2 \text{ s}^{-1}$ for CM (a) and $k_p = 1.0 \times 10^{-17} \text{ m}^2 \text{ s}^{-1}$, $D_{Cr} = 4.7 \times 10^{-16} \text{ m}^2 \text{ s}^{-1}$ for AM (b) and AM-HR (c). For AM alloy (b), full symbols denote AM-Z while empty ones denote measurements for AM-Y.

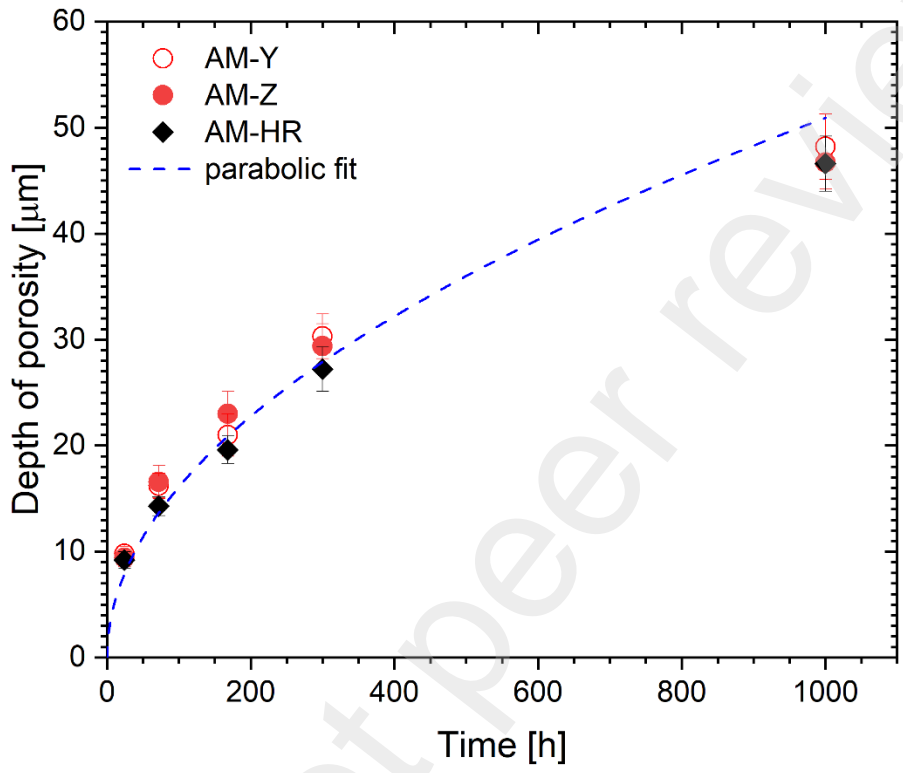
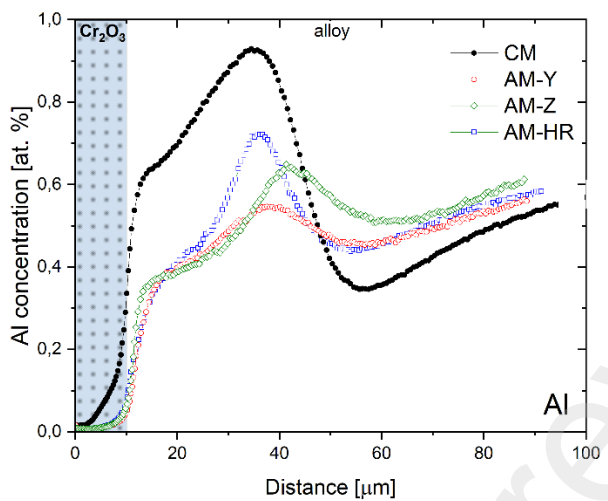
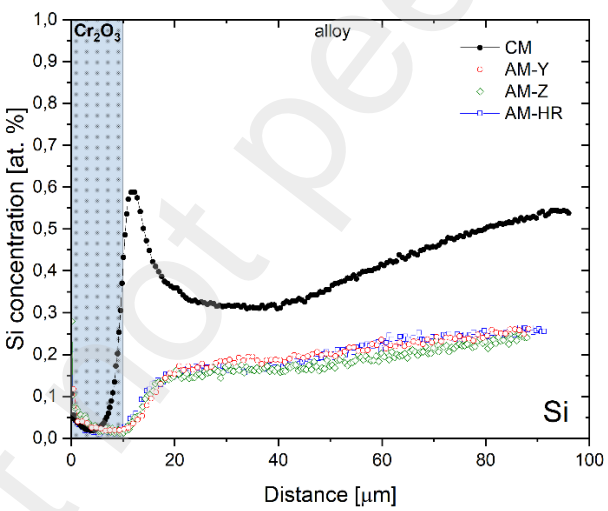


Figure 10: Kinetics of void propagation in the subsurface metal during air exposure of AM and hot-rolled alloy IN625 in air at 900 °C. The measurements (symbols) are fitted (line) with a parabolic time dependence, $k_p^{voids} = 3.5 \times 10^{-16} \text{ m}^2 \text{ s}^{-1}$.



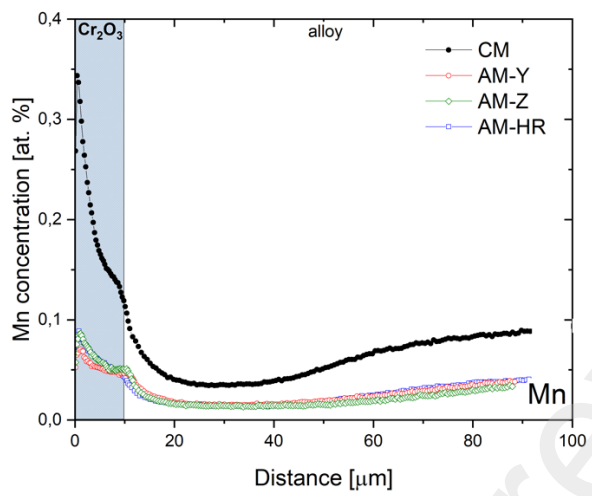
(a)



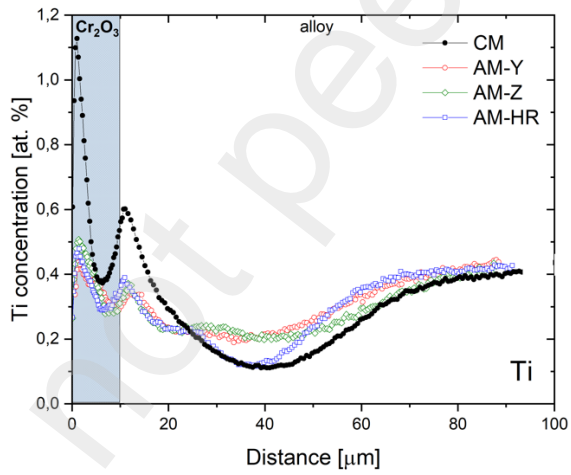
(b)

Figure 11: GD-OES concentration profiles of (a) Al, (b) Si, (c) Mn and (d) Ti in CM and AM alloy IN625 after 1000 h of air exposure at 900 °C

Figure 11 – continued



(c)



(d)

Figure 11: GD-OES concentration profiles of (a) Al, (b) Si, (c) Mn and (d) Ti in CM and AM alloy IN625 after 1000 h of air exposure at 900°C.

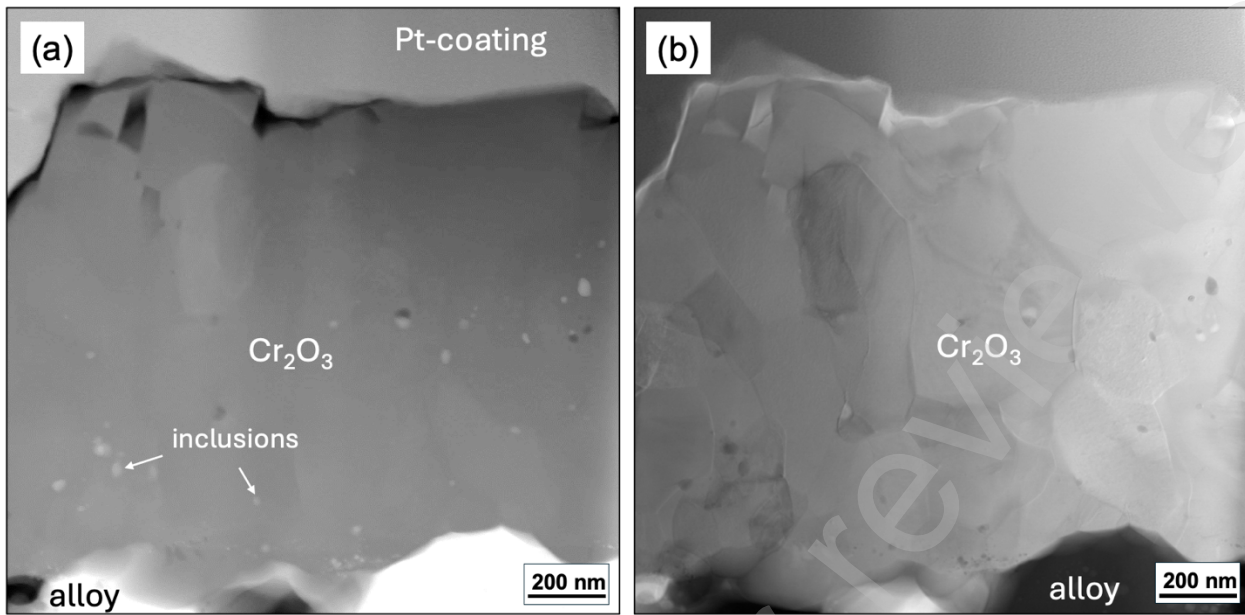


Figure 12: HAADF (a) and BF (b) TEM images of the oxide scale grown on AM-Y after 24 h exposure in air at 900 °C.

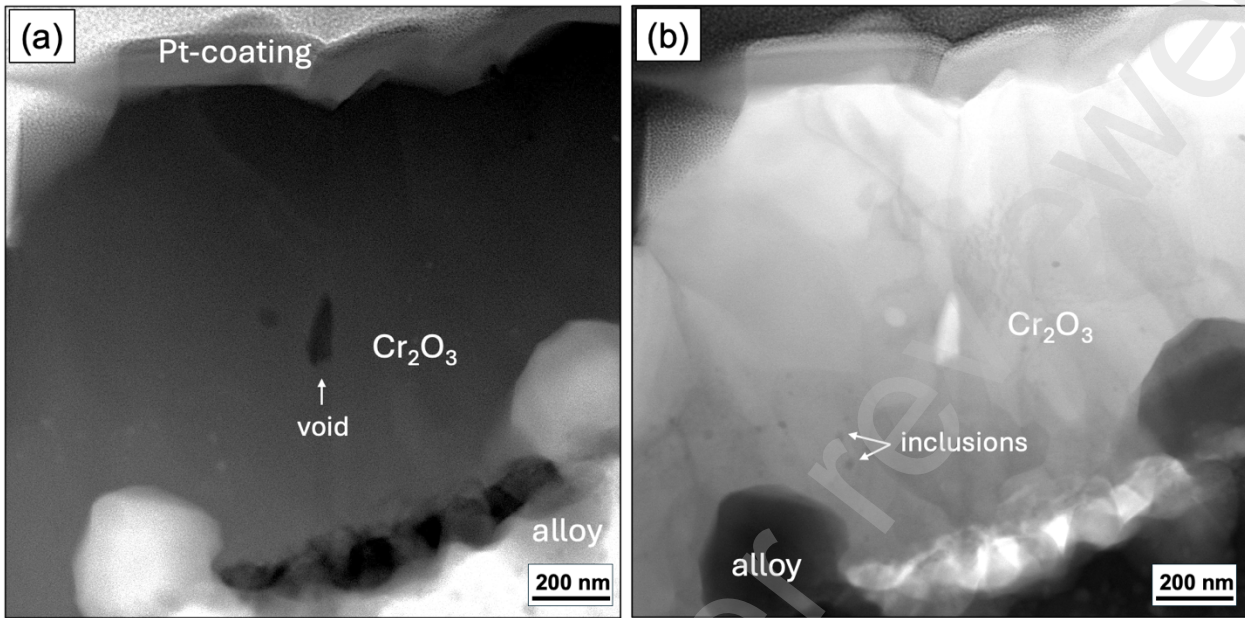


Figure 13: HAADF (a) and BF (b) TEM images of the oxide scale grown on CM after 24 h exposure in air at 900 °C.

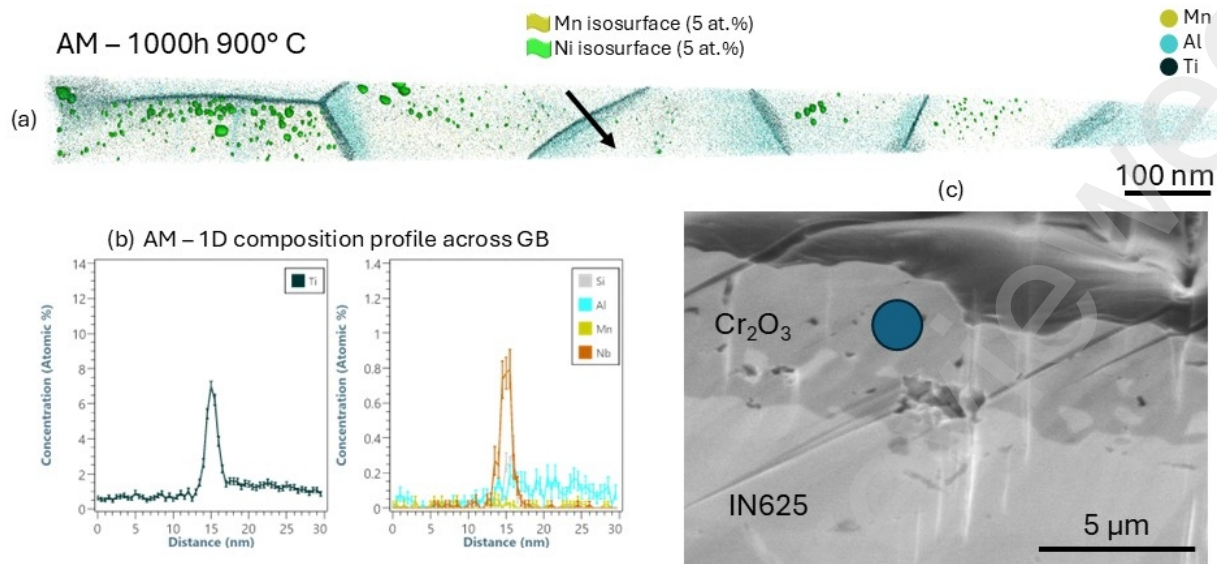


Figure 14: APT reconstruction of chromia scale grown on AM-Y after 1000 h air exposure at 900 °C. An overview of the full run is presented in (a). The arrow indicates the location and direction of the 1D composition profile across the grain boundary plotted in (b). The lift-out site from which the specimen was obtained is presented in (c)

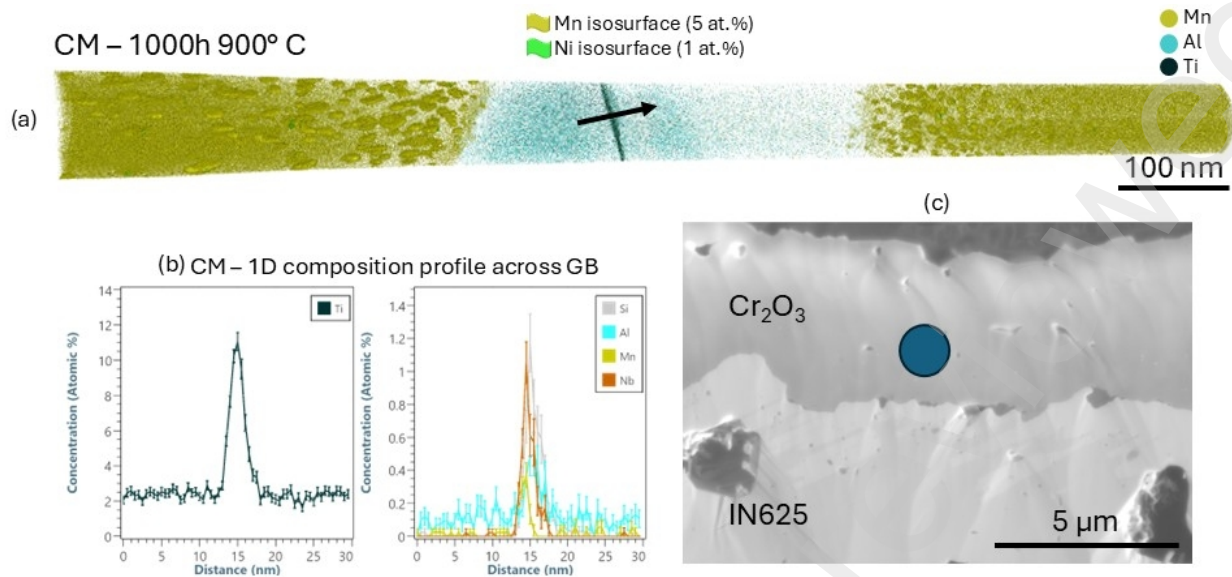


Figure 15 : APT reconstruction of chromia scale grown on CM IN625 after 1000 h air exposure at 900 °C. An overview of the full run is presented in (a). The arrow indicates the location and direction of the 1D composition profile across the grain boundary plotted in (b). The lift-out site from which the specimen was obtained is presented in (c)

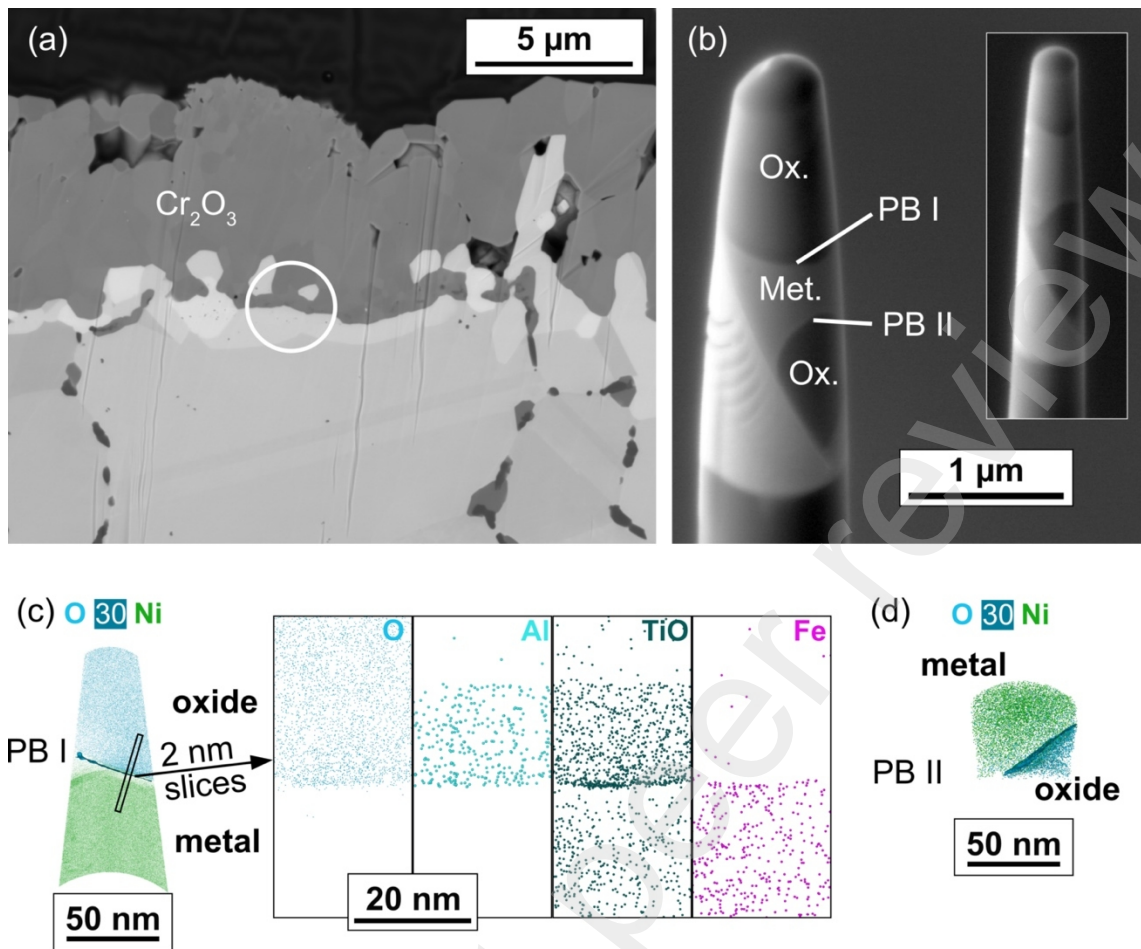
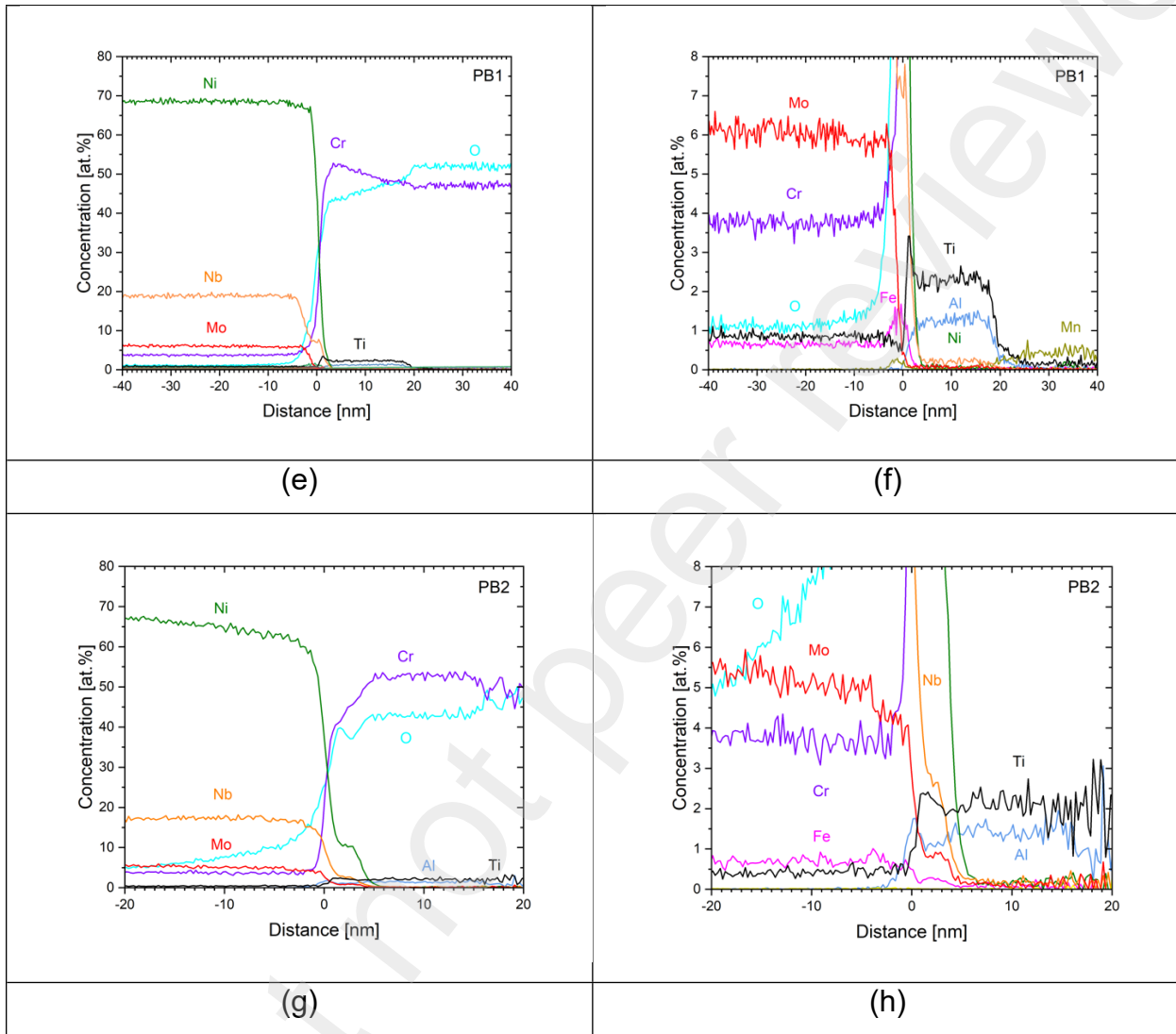


Figure 16: APT reconstruction of oxide-metal interfaces in the Cr_2O_3 scale thermally grown on CM after 1000 h air exposure at 900 °C. Figures (a) and (b) the sampling site, (c) and (d) APT reconstructions, (e,f) and (g,h) element concentration profiles across the interface

Figure 16 - continued



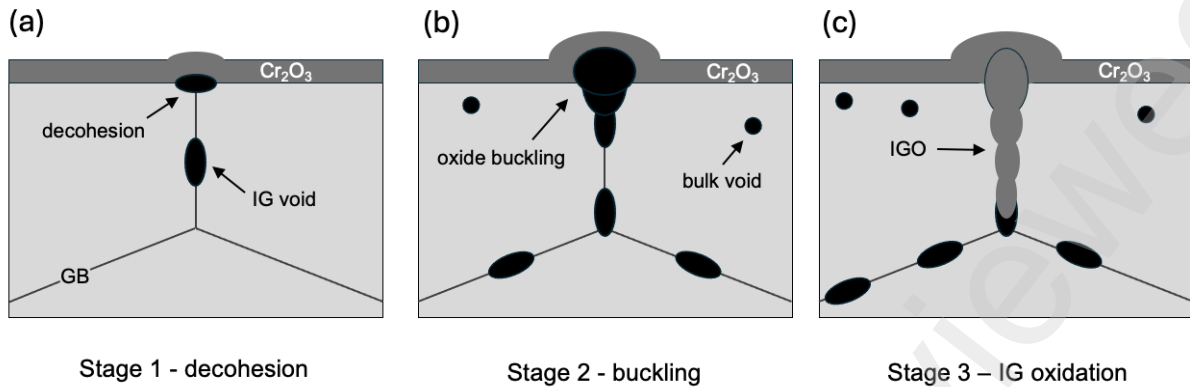


Figure 17: Schematic illustrating the evolution of intergranular oxidation (IGO) attack during oxidation of AM alloy IN625: a) Stage 1 - formation of Kirkendall voids at GBs and initial oxide scale decohesion; b) Stage 2 - oxide buckling and growth of the IG void; c) Stage 3 - oxide cracking and oxidation of the IG void.

TABLES

Table 1: Chemical composition of CM and AM alloy IN625 determined by ICP-OES and IR [wt.%]

Alloy	Ni	Cr	Mo	Nb	Fe	Mn	Ti	Al	Si	C
CM IN625	Bal.	21.6	8.9	3.5	3.6	0.11	0.33	0.32	0.27	0.02
AM IN625	Bal.	21.5	8.7	3.9	0.8	0.04	0.38	0.28	0.12	0.01

Table 2: Kinetic parameters of oxidation and Cr depletion in CM and AM alloy IN625 during air oxidation at 900 °C: experimental parabolic rate constants and calculated interdiffusion coefficient of Cr in the alloy.

Experimental values				Wagnerian calculation	
	$k_p^{Cr_2O_3}$ [m ² s ⁻¹]			$k_p^{Cr_2O_3}$ [m ² s ⁻¹]	\tilde{D}_{Cr} [m ² s ⁻¹]
	Thermogravimetry		Microscopy		
	short-term up to 72h	long-term up to 1000h	long-term up to 1000h		
CM	9.1×10^{-18}	5.0×10^{-18}	5.5×10^{-18}	5.5×10^{-18}	2.5×10^{-16}
AM-Y	1.9×10^{-17}	9.6×10^{-18}	4.1×10^{-18}	1.0×10^{-17}	4.7×10^{-16}
AM-Z	2.1×10^{-17}	9.9×10^{-17}	4.4×10^{-18}	1.0×10^{-17}	4.7×10^{-16}
AM-HR	2.7×10^{-17}	1.1×10^{-17}	5.5×10^{-18}	1.0×10^{-17}	4.7×10^{-16}

Table 3: Comparison of experimentally determined values of parabolic rate constant $k_p^{Cr_2O_3}$ for oxidation of CM alloy IN625 in air at 900°C with the data available in literature differentiating in-situ exposures in thermobalance and long-term furnace experiments. The $k_p^{Cr_2O_3}$ values were calculated in terms of oxide thickness using Eqn. (1).

Short-term experiments in thermobalance		Long-term furnace exposures	
Source	$k_p^{Cr_2O_3}$ [m ² s ⁻¹]	Source	$k_p^{Cr_2O_3}$ [m ² s ⁻¹]
this work	9.1×10^{-18}	this work	5.0×10^{-18}
Rammenate et al. [15]	7.2×10^{-18}	Duthoit et al. [41]	5.5×10^{-18}
Contri et al. [31]	7.3×10^{-18}	Pindea-Arriga et al. [16]	5.4×10^{-18}

References

1. Reed RC. *The Superalloys*. Cambridge University Press; 2006. doi:10.1017/CBO9780511541285.
2. Murr LE. Metallurgy of additive manufacturing: Examples from electron beam melting. *Addit Manuf.* 2015;5:40–53.
3. Frazier WE. Metal Additive Manufacturing: A Review. *J Mater Eng Perform.* 2014;23:1917–1928.
4. DebRoy T, Wei HL, Zuback JS, et al. Additive manufacturing of metallic components – Process, structure and properties. *Prog Mater Sci.* 2018;92:112–224.
5. Karmuhilan M, Kumanan S. A Review on Additive Manufacturing Processes of Inconel 625. *J Mater Eng Perform.* 2022;31:2583–2592.
6. Gao S, Li Z, Van Petegem S, et al. Additive manufacturing of alloys with programmable microstructure and properties. *Nature Communications* 2023 14:1. 2023;14:1–11.
7. Son K, Kassner ME, Lee KA. The Creep Behavior of Additively Manufactured Inconel 625. *Adv Eng Mater.* 2020;22.
8. Son K-T, Phan TQ, Levine LE, et al. The creep and fracture properties of additively manufactured inconel 625. *Materialia (Oxf).* 2021;15:101021.
9. de Leon Nope G, Wang G, Alvarado-Orozco JM, Gleeson B. Role of Elemental Segregation on the Oxidation Behavior of Additively Manufactured Alloy 625. *JOM.* 2022;74:1698–1706.
10. de Leon Nope G, Wang G, Alvarado-Orozco JM, Gleeson B. Effects of High-Temperature Oxidation on Fatigue Life of Additive-Manufactured Alloy 625. *Minerals, Metals and Materials Series.* 2023;249–269. doi:10.1007/978-3-031-27447-3_17/FIGURES/9.
11. de Leon Nope G, Wang G, Gleeson B. Influence of Alloy 625 Manufacturing Process on 950 °C Oxidation Behavior in Air and Post-oxidation High-Cycle Fatigue Performance. *High Temperature Corrosion of Materials.* 2024;1–13. doi:10.1007/S11085-024-10286-3/FIGURES/6.
12. Chyrkin A, Gunduz KO, Fedorova I, et al. High-temperature oxidation behavior of additively manufactured IN625: Effect of microstructure and grain size. *Corros Sci.* 2022;205.
13. Chyrkin A, Nowak WJ, Gunduz KO, et al. Intergranular oxidation of additively manufactured Ni-base alloy 625: The role of Si. *Corros Sci.* 2023;219:111234.
14. Parizia S, Marchese G, Rashidi M, et al. Effect of heat treatment on microstructure and oxidation properties of Inconel 625 processed by LPBF. *J Alloys Compd.* 2020;846:156418.
15. Ramenatte N, Vernouillet A, Mathieu S, Vande Put A, Vilasi M, Monceau D. A comparison of the high-temperature oxidation behaviour of conventional wrought and laser beam melted Inconel 625. *Corros Sci.* 2020;164.
16. Pineda-Arriaga KY, Ramírez-Ramírez JH, Pérez-González FA, Alvarado-Orozco JM, Colás R, Garza-Montes-de-Oca NF. Oxidation in Water Vapor of Inconel 625 Fabricated by Additive Manufacturing. *High Temperature Corrosion of Materials.* 2024;101:1–11.

17. Pineda-Arriaga KY, Ramírez-Ramírez JH, Pérez-González FA, Alvarado-Orozco JM, Colás R, Garza-Montes-de-Oca NF. Characterization of the High-Temperature Oxidation Behavior of Inconel 625® Fabricated by Additive Manufacturing and Conventional Methods. *Oxidation of Metals*. 2022;98:489–510.
18. Condruz MR, Matache G, Paraschiv A, Badea T, Badilita V. High Temperature Oxidation Behavior of Selective Laser Melting Manufactured IN 625. *Metals (Basel)*. 2020;10:668.
19. Sharifitabar M, Khorshahian S, Shafiee Afarani M, Kumar P, Jain NK. High-temperature oxidation performance of Inconel 625 superalloy fabricated by wire arc additive manufacturing. *Corros Sci*. 2022;197:110087.
20. Lewis ER, Taylor MP, Attard B, et al. Microstructural characterisation and high-temperature oxidation of laser powder bed fusion processed Inconel 625. *Mater Lett*. 2022;311:131582.
21. Andrade BW, Mariani FE, Coelho RT, de Sousa Malafaia AM. Comparison of the Oxidation Behavior at High Temperature of INCONEL 625 Forged and Produced by Additive Manufacturing. *High Temperature Corrosion of Materials*. 2024;1–14. doi:10.1007/S11085-024-10283-6/FIGURES/9.
22. Sanvienvongsak T, Monceau D, Desgranges C, Macquaire B. Intergranular oxidation of Ni-base alloy 718 with a focus on additive manufacturing. *Corros Sci*. 2020;170:108684.
23. Sanvienvongsak T, Monceau D, Macquaire B. High temperature oxidation of IN 718 manufactured by laser beam melting and electron beam melting: Effect of surface topography. *Corros Sci*. 2018;141:127–145.
24. Sanvienvongsak T, Monceau D, Madelain M, Desgranges C, Smialek J, Macquaire B. Cyclic oxidation of alloy 718 produced by additive manufacturing compared to a wrought-718 alloy. *Corros Sci*. 2021;192:109804.
25. Calandri M, Manfredi D, Calignano F, et al. Solution Treatment Study of Inconel 718 Produced by SLM Additive Technique in View of the Oxidation Resistance. *Adv Eng Mater*. 2018;20:1800351.
26. Chyrkin A, Huczkowski P, Shemet V, Singheiser L, Quadakkers WJ. Sub-scale depletion and enrichment processes during high temperature oxidation of the nickel base alloy 625 in the temperature range 900–1000 °c. *Oxidation of Metals*. 2011;75.
27. Pfeifer J-P, Holzbrecher H, Quadakkers WJ, Breuer U, Speier W. Quantitative analysis of oxide films on ODS-alloys using MCs+-SIMS and e-beam SNMS. *Fresenius J Anal Chem*. 1993;346:186–191.
28. Quadakkers WJ, Elschner A, Speier W, Nickel H. Composition and growth mechanisms of alumina scales on FeCrAl-based alloys determined by SNMS. *Appl Surf Sci*. 1991;52:271–287.
29. Nowak WJ. Characterization of oxidized Ni-based superalloys by GD-OES. *J Anal At Spectrom*. 2017;32:1730–1738.
30. Thompson K, Lawrence D, Larson DJ, Olson JD, Kelly TF, Gorman B. In situ site-specific specimen preparation for atom probe tomography. *Ultramicroscopy*. 2007;107:131–139.

31. Contri B, Valette S, Soustre M, Lefort P. Inconel®625 oxidation in CO₂: Kinetics and reaction mechanism. *Corros Sci.* 2023;217:111101.
32. Choi N, da Silva Pinto M, Yang S, et al. Grain boundary diffusion in additively manufactured CoCrFeMnNi high-entropy alloys: Impact of non-equilibrium state, temperature and relaxation. *Materialia (Oxf).* 2024;38:102228.
33. Wagner C. Oxidation of Alloys Involving Noble Metals. *J Electrochem Soc.* 1956;103:571.
34. Bastow BD, Whittle DP, Wood GC. Alloy depletion profiles resulting from the preferential removal of the less noble metal during alloy oxidation. *Oxidation of Metals.* 1978;12:413–438.
35. Pillai R, Romedenne M, Haynes JA, Pint BA. Oxidation Behavior of Candidate NiCr Alloys for Engine Exhaust Valves: Part I—Effect of Minor Alloying Elements. *Oxidation of Metals.* 2021;95:157–187.
36. Vayyala A, Povstugar I, Naumenko D, Quadakkers WJ, Hattendorf H, Mayer J. A Nanoscale Study of Thermally Grown Chromia on High-Cr Ferritic Steels and Associated Oxidation Mechanisms. *J Electrochem Soc.* 2020;167:061502.
37. Vayyala A, Povstugar I, Naumenko D, Quadakkers WJ, Hattendorf H, Mayer J. Effect of gas composition on the oxide scale growth mechanisms in a ferritic steel for solid oxide cell interconnects. *Corros Sci.* 2023;221:111317.
38. Mayweg D, Eriksson J, Sattari M, Andrén HO, Thuvander M. Corrosion of zirconium fuel cladding inside a boiling water reactor: A post-irradiation study by atom probe tomography. *Acta Mater.* 2025;292:121020.
39. Bachhav M, Pawar G, Vurpillot F, et al. Interpreting the Presence of an Additional Oxide Layer in Analysis of Metal Oxides-Metal Interfaces in Atom Probe Tomography. *Journal of Physical Chemistry C.* 2019;123:1313–1319.
40. Jakob S, Fazi A, Thuvander M. Laser-Assisted Field Evaporation of Chromia with Deep Ultraviolet Laser Light. *Microscopy and Microanalysis.* 2025;31.
41. Duthoit G, Vande Put A, Caussat B, Vergnes H, Monceau D. Influence of Water Vapor and Local Gas Velocity on the Oxidation Kinetics of In625 at 900 °C: Experimental Study and CFD Gas Phase Simulation. *High Temperature Corrosion of Materials.* 2024;101:1513–1526.
42. Naumenko D, Gleeson B, Wessel E, Singheiser L, Quadakkers WJ. Correlation between the microstructure, growth mechanism, and growth kinetics of alumina scales on a FeCrAlY alloy. *Metall Mater Trans A Phys Metall Mater Sci.* 2007;38 A:2974–2983.
43. Romedenne M, Pillai R, Dryepondt S, Pint BA. Effect of Water Vapor on Lifetime of 625 and 120 Foils During Oxidation Between 650 and 800 °C. *Oxidation of Metals.* 2021;96:589–612.
44. Buscail H, Rolland R, Issartel C, et al. Effects of water vapour on the oxidation of a nickel-base 625 alloy between 900 and 1,100 °C. *J Mater Sci.* 2011;46:5903–5915.
45. Garcia-Fresnillo L, Chyrkin A, Böhme C, Barnikel J, Schmitz F, Quadakkers WJ. Oxidation behaviour and microstructural stability of alloy 625 during long-term exposure in steam. *J Mater Sci.* 2014;49.

46. Huczkowski P, Lehnert W, Angermann H-H, et al. Effect of gas flow rate on oxidation behaviour of alloy 625 in wet air in the temperature range 900–1000 °C. *Materials and Corrosion*. 2017;68.
47. Zurek J, Young DJ, Essuman E, et al. Growth and adherence of chromia based surface scales on Ni-base alloys in high- and low-pO₂ gases. *Materials Science and Engineering A*. 2008;477:259–270.
48. Hansel M, Shemet V, Turan E, et al. Scaling Kinetics and Scale Microstructure of Chromia Scales Formed on Ni-25%Cr Model Alloy during Oxidation in H₂O-Containing High and Low pO₂ Test Gas at 1000 C. *ECS Trans*. 2015;66:1–21.
49. Vayyala A, Povstugar I, Galiullin T, et al. Effect of Nb Addition on Oxidation Mechanisms of High Cr Ferritic Steel in Ar–H₂–H₂O. *Oxidation of Metals*. 2019;92:471–491.
50. Barth TL, Marquis EA. The Effect of Ti on the Early Stages of Oxidation of an Alumina-Forming NiCrAl Alloy. *Oxidation of Metals*. 2019;92:13–26.
51. Wang G, Ouyang H, Fan C, et al. The origin of high-density dislocations in additively manufactured metals. *Mater Res Lett*. 2020;8:283–290.
52. Hu D, Grilli N, Yan W. Dislocation structures formation induced by thermal stress in additive manufacturing: Multiscale crystal plasticity modeling of dislocation transport. *J Mech Phys Solids*. 2023;173:105235.
53. Li Z, Cui Y, Yan W, et al. Enhanced strengthening and hardening via self-stabilized dislocation network in additively manufactured metals. *Materials Today*. 2021;50:79–88.
54. Love GR. Dislocation pipe diffusion. *Acta Metallurgica*. 1964;12:731–737.
55. Mimkes J. Pipe diffusion along isolated dislocations. *Thin Solid Films*. 1975;25:221–230.
56. Romedenne M, Pillai R, Kirka M, Dryepondt S. High temperature air oxidation behavior of Hastelloy X processed by Electron Beam Melting (EBM) and Selective Laser Melting (SLM). *Corros Sci*. 2020;171:108647.
57. Romedenne M, Stack P, Pillai R, Dryepondt S. Isothermal and Cyclic Oxidation of Haynes 282 Processed by Electron Beam Melting (EBM) and Laser Powder Bed Fusion (LPBF) in Dry Air at 800 and 950 °C. *JOM*. 2022;74:1–12.
58. Siri C, Popa I, Vion A, Langlade C, Chevalier S. Impact of Selective Laser Melting Additive Manufacturing on the High Temperature Behavior of AISI 316L Austenitic Stainless Steel. *Oxidation of Metals*. 2020;94:527–548.
59. Siri C, Popa I, Vion A, Langlade C, Chevalier S. Impact of Water Vapor on the High Temperature Oxidation of Wrought and Selective Laser Melted (SLM) AISI 316L. *Oxidation of Metals*. 2021;96:347–359.
60. Gheno T, Rio C, Rimpot E, Mercier S. Kinetics of Alloy Depletion During Selective Oxidation in Polycrystals. *High Temperature Corrosion of Materials*. 2023;100:709–743.
61. Leistikow S, Wolf I, Grabke HJ. Effect of cold work on the oxidation behavior and carburization resistance of Alloy 800. *Werkstoffe und Korrosion*. 1987;38:556–562.

62. Caplan D. Effect of cold work on the oxidation of FeCr alloys in water vapour at 600°C. *Corros Sci.* 1966;6:509–515.
63. Kundin J, Riyahi khorasgani A, Schiedung R, Camin B, Steinbach I. Modeling vacancy-induced porosity in compositionally-graded complex alloys. *Acta Mater.* 2024;271:119905.
64. Riyahi khorasgani A, Steinbach I, Camin B, Kundin J. A phase-field study to explore the nature of the morphological instability of Kirkendall voids in complex alloys. *Scientific Reports* 2024 14:1. 2024;14:1–17.
65. Yamaura S, Igarashi Y, Tsurekawa S, Watanabe T. Structure-dependent intergranular oxidation in Ni–Fe polycrystalline alloy. *Acta Mater.* 1999;47:1163–1174.
66. Trindade VB, Krupp U, Wagenhuber PhE-G, Virkar YM, Christ H-J. Studying the role of the alloy-grain-boundary character during oxidation of Ni-base alloys by means of the electron back-scattered diffraction technique. *Materials at High Temperatures*. 2005;22:207–212.
67. RHINES FN, WOLF JS. ROLE OF OXIDE MICROSTRUCTURE AND GROWTH STRESSES IN THE HIGH-TEMPERATURE SCALING OF NICKEL. *Met Trans.* 1970;1:1701–1710.
68. Evans HE. Stress effects in high temperature oxidation of metals. *International Materials Reviews*. 1995;40:1–40.
69. Quadakkers WJ, Huczkowski P, Naumenko D, et al. Why the Growth Rates of Alumina and Chromia Scales on Thin Specimens Differ from those on Thick Specimens. *Materials Science Forum*. 2008;595–598:1111–1118.
70. Asensio-Jimenez C, Niewolak L, Hattendorf H, et al. Effect of Specimen Thickness on the Oxidation Rate of High Chromium Ferritic Steels: The Significance of Intrinsic Alloy Creep Strength. *Oxidation of Metals*. 2013;79:15–28.
71. Wei FI, Stott FH. The development of Cr₂O₃ scales on iron-chromium alloys containing reactive elements. *Corros Sci.* 1989;29:839–861.
72. Caplan D, Harvey A, Cohen M. Oxidation of chromium at 890°–1200°C. *Corros Sci.* 1963;3:161–IN8.
73. Whittle DP, Stringer J. Improvements in high temperature oxidation resistance by additions of reactive elements or oxide dispersions. *Philosophical Transactions of the Royal Society of London. Series A, Mathematical and Physical Sciences*. 1980;295:309–329.
74. Hou PY, Stringer J. The effect of aluminum as an alloying addition or as an implant on the high-temperature oxidation of Ni-25Cr. *Oxidation of Metals*. 1990;34:299–321.
75. Pint BA. Progress in understanding the reactive element effect since the Whittle and Stringer literature review. In: *John Stringer Symposium on High Temperature Corrosion*. 2001.9–19.
76. Desgranges C, Lequien F, Aublant E, Nastar M, Monceau D. Depletion and voids formation in the substrate during high temperature oxidation of Ni-Cr alloys. *Oxidation of Metals*. 2013;79:93–105.